DEVELOPMENT OF A FINITE ELEMENT MODEL FOR PREDICTING THE IMPACT ENERGY ABSORBING PERFORMANCE OF A COMPOSITE STRUCTURE

A Thesis

presented to

the Faculty of California Polytechnic State University,

San Luis Obispo

In Partial Fulfillment

of the Requirements for the Degree

Master of Science in Mechanical Engineering

by

Matthew Lowell Roberts

June 2014

COMMITTEE MEMBERSHIP

TITLE:	Development of a Finite Element Model for Predicting the Impact Energy Absorbing Performance of a Composite Structure
AUTHOR:	Matthew Lowell Roberts
DATE SUBMITTED:	June 2014

COMMITTEE CHAIR:	Joseph Mello, Ph.D. Professor of Mechanical Engineering Cal Poly, San Luis Obispo
COMMITTEE MEMBER:	Peter Schuster, Ph.D. Professor of Mechanical Engineering Cal Poly, San Luis Obispo
COMMITTEE MEMBER:	Eltahry Elghandour, Ph. D. Lecturer of Aerospace Engineering Cal Poly, San Luis Obispo

ABSTRACT

Development of a Finite Element Model for Predicting the Impact Energy Absorbing Performance of a Composite Structure

Matthew Lowell Roberts

Because of their high strength-to-weight ratio, Fiber Reinforced Composite (FRC) materials are well suited for use in high performance racing applications where weight must be kept to a minimum. Formula SAE (FSAE) race cars are designed and built by college students, roughly following the model of a scaled down Formula One car. Strict regulations are placed on specific components of the car in the interest of equalizing competition and ensuring the safety of the drivers. Students are required to construct a survival cell (the chassis), which can resist large amounts of energy in the event of a crash, with an energy absorbing device at the front of the vehicle. The nose cone of the Cal Poly FSAE car is constructed as a carbon fiber shell designed to act as this sacrificial energy absorbing device. One difficulty associated with using FRC materials is that the anisotropic properties can lead to a variety of complex failure modes such as buckling, delamination, matrix cracking, and fiber breakage, all of which absorb different amounts of energy. In order to accurately predict the behavior of the nose cone so that it meets the requirements set forth by SAE, an initial finite element model has been constructed. This model uses the test results from another paper to construct an explicit non-linear dynamic analysis in Abaqus which simulates the axial crushing of a thin walled composite tube between two rigid plates. The modeling techniques discussed in this paper will be used as the basis for a future thesis dedicated to designing the nose cone for the Cal Poly FSAE car.

TABLE OF CONTENTS

LIST OF TABLES

LIST OF FIGURES

GLOSSARY OF VARIABLES

σ: stress
τ: shear stress
ε: strain
γ: shear strain
E: Young's modulus
ν: Poisson's ratio
G: shear modulus
κ: curvature
P_{cr}: critical load
[M]: mass matrix
[C]: damping matrix
[K]: stiffness matrix
u: displacement
$\dot{u}$: velocity
$\ddot{u}$: acceleration
e: error
r: residual
t: time
f: force
F_{FT}: damage initiation variable for fiber tensile direction
F_{FC}: damage initiation variable for fiber compressive direction
F_{MT}: damage initiation variable for matrix tensile direction
F_{MC}: damage initiation variable for matrix compressive direction
$\hat{\sigma}_{11}$: effective stress, fiber (longitudinal) direction
$\hat{\sigma}_{22}$: effective stress, matrix (transverse) direction
$\hat{\sigma}_{12}$: effective shear stress
S_{FT}: ultimate strength, fiber tension
S_{FC}: ultimate strength, fiber compression
S_{MT}: ultimate strength, matrix tension
S_{MC}: ultimate strength, matrix compression
τ_F: fiber (longitudinal) shear strength
τ_M: matrix (transverse) shear strength
d_f: damage evolution variable, fiber (longitudinal) direction
d_m: damage evolution variable, matrix (transverse) direction
d_s: damage evolution variable, shear
d_{max}: upper limit of damage evolution variable. Element is deleted once this is reached
δ_{eq}^{ft}: equivalent displacement, fiber tension
δ_{eq}^{fc}: equivalent displacement, fiber compression
δ_{eq}^{mt}: equivalent displacement, matrix tension
δ_{eq}^{mc}: equivalent displacement, matrix compression
δ_{eq}^{o}: equivalent displacement at the onset of damage
δ_{eq}^{F}: equivalent displacement at failure

σ_{eq}^{ft}: equivalent stress, fiber tension
σ_{eq}^{fc}: equivalent stress, fiber compression
σ_{eq}^{mt}: equivalent stress, matrix tension
σ_{eq}^{mc}: equivalent stress, matrix compression
G^C: total energy dissipated during damage

Chapter 1. Introduction

The Formula SAE (FSAE) team at Cal Poly, San Luis Obispo recently switched from a steel tube space frame for their car to a hybrid monocoque design. The front half of the car is a carbon fiber tub which serves as the main load-frame structure for the entire vehicle. Behind that, a steel subframe is bolted on which houses the drivetrain and rear suspension. By replacing the front of the steel frame with the carbon fiber tub, the team was able to drastically reduce the overall weight of the car while simultaneously increasing its torsional stiffness. An additional design change which accompanied the tub was incorporating the mandatory impact attenuator into the design of the nose cone.

The impact attenuator has several requirements placed on its design by SAE to ensure the safety of the driver in the event of a crash. Those requirements are listed below [1].

- Able to decelerate a 300 kg vehicle with an initial velocity of 7.0 m/s
- Average deceleration cannot exceed 20 g's
- Peak deceleration cannot exceed 40 g's
- Total energy absorbed must meet or exceed 7350 Joules
- At least 200 mm long, with its length oriented along the fore/aft axis of the frame

In previous years, a pre-approved impact attenuator would be purchased and the nose cone would simply act as an aesthetic/aerodynamic cover. This new design called for the nose cone itself to act as the impact attenuator. Fiber reinforced composites (FRCs), such as carbon fiber, are excellent candidates for sacrificial energy absorbing devices because their complex failure modes are capable of absorbing large amounts of

energy. At the same time, analyzing and accurately predicting their behavior is extremely difficult.

The advent of Finite Element (FE) modeling has allowed engineers to evaluate their designs without needing to build a physical prototype, which can quickly become very expensive after just a few iterations. Cal Poly's FSAE team currently builds and tests multiple nose cones before arriving at the final design. With such high costs associated with this process and a tight budget, the team needs a better way to evaluate their nose cone designs. The purpose of this paper is to outline the process for creating an FE model using Abaqus Explicit to accurately predict the impact behavior of the nose cone attenuator without the need to physically build one. The model is constructed based upon a physical specimen tested by Huang and Wang [2] and the FE results are compared to the results from their experiments. A simple tube geometry consisting of 14 layers of unidirectional carbon fiber reinforced polymer (CFRP) is defined and analyzed, but the techniques presented will provide a guide for later adaptation to the more complex geometry and layup schedule of the actual nose cone.

1.1 Literature Review

Numerous papers have been written in recent years studying the effectiveness of using composite materials in impact energy absorbing roles. Racing teams from Formula One performed much of this research in the interest of meeting strict safety regulations placed on their vehicles. Several studies [3-6] all showcase the importance of designing these energy absorbing structures to have a progressive failure mode. The main failure modes demonstrated are fiber and matrix breakage. Some delamination and buckling occurs, but the majority of the energy absorbed is due to the brittle material failure

behavior. Finite element models were also constructed to predict the material response, all of which used the Tsai-Wu failure criteria implemented in LS-DYNA.

Other FSAE teams have also experimented with composite impact attenuators. Politecnico de Torino in Italy used an aluminum attenuator previously [7] and decided to switch to a composite attenuator [8-10] in order to save weight on their vehicle. A finite element model was built in LS-DYNA using the Tsai-Wu failure criteria. Good agreement was achieved between their numerical models and experimental results both with a simple tube geometry and with the 3D nose cone shape. Difficulties associated with modeling the complex failure modes led to the numerical model predicting more buckling than fiber breakage, although the forces predicted still closely matched those from the physical tests.

The composite structures being crushed exhibited two distinct behaviors throughout the papers researched. The first behavior was one which produced an initial spike in the load-displacement response followed by a stable crush zone at a lower force value [2,3,10-13]. Figure 1 demonstrates this behavior.

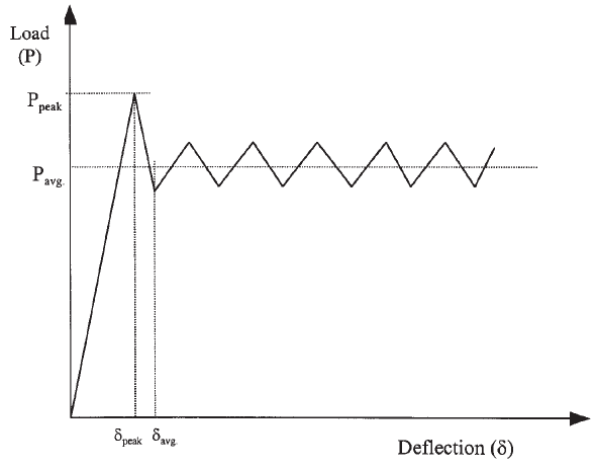

Figure 1. Key Parameters in Energy Absorbing Tests [11].

The specimens in these papers failed by a combination of material damage and local buckling. Since the brittle material failure should exhibit an even and sustained crushing load, the initial spike is most likely due to the force required to initiate buckling. The second behavior demonstrated was similar to the first but without the initial spike [6]. Tube specimens which displayed this behavior either had smaller diameters or an initiator built into the impacting plate and experienced no local or global buckling.

Abdel-Haq and Newaz [11] studied the role of different failure modes on the energy absorption capabilities of composite tubes. Their efforts were focused on controlling the crushing in order to reduce the difference between the peak load required to initiate crushing and the load required to continue crushing the tube. Experiments were performed on unidirectional tubes with an added hoop constraint in the form of a steel tube that slid longitudinally with the crush zone. It was noted that the extra hoop support did not allow cracks to propagate far ahead of the crush zone. Reducing the crack length along the longitudinal axis of the tube shortened the distance the crack had to travel initially, therefore lowering the initial load spike observed. The reduced length also made for shorter “fronds” which required greater force in order to generate the same moment on them. These shorter fronds are what generated the higher average load during sustained crushing.

1.2 Thesis Paper Overview

One of the main goals of this thesis is to provide a guide for constructing a finite element model to predict the behavior of a composite structure. In order for the reader to better understand both composite design and finite element analysis, chapters 2-4 in this

paper provide an overview of these topics. These chapters are meant to be general overviews to illustrate the techniques used independent from the specific application. Later sections will address how these topics apply to the composite tube problem presented in this paper.

No physical tests were performed during the course of this thesis. In lieu of first hand real-world test data, published results from another experiment were used to validate the FE model. This experiment was performed by Huang and Wang and can be found in reference [2] along with the specific material properties, layup, modeling techniques, and test procedures. These results are presented in this thesis as the "physical results." The physical results are meant to be different than the "physical predictions" also discussed. In this thesis, "physical predictions" refer to the failure behavior of the structure as predicted by an FE model. There is one set of physical results, just from the paper. There are two sets of physical predictions, one from the paper and one from this thesis.

Chapter 2. Fiber Reinforced Composites

2.1 Basic Overview

Fiber reinforced composites (FRCs) consist of a fibrous material held in place by some sort of matrix. The main role of the matrix is to hold the fibers in place; its strength is orders of magnitude less than that of the fibers [14]. For the purpose of this paper, carbon fiber (CF) will be the focus of the discussion even though there are many other examples of FRC materials. The specific type of CF being examined falls into the category of unidirectional continuous fiber composites. These types of composites consist of long, unbroken fibers all oriented in the same direction. As with all FRC materials of this type, CF is very strong when loaded in the direction of the fibers (longitudinally). However, the material is significantly weaker when loaded in the direction perpendicular to the fibers (transversely) because the load is carried predominately by the matrix instead of the fibers.

Table 1. General Strength and Stiffness Comparison [14,15]

Material	Tensile Modulus, E (GPa)	Tensile Strength, σ_u (MPa)	Specific Modulus, E/ρ (m)	Specific Strength, σ_u/ρ (m)
CF Longitudinal	186	2410	12.4	148
CF Transverse	9.31	55.2	.622	3.38
Steel	207	338 – 2100	2.69	4.39 – 27.4
Aluminum	68.9	138 – 621	2.62	5.23 – 23.6

The orthotropic behavior of CF requires that parts be constructed by stacking multiple unidirectional laminae on top of each other in order to obtain the necessary strength in the direction of stress in the laminate.

2.2 Applications

Composite materials have been around for decades, but their use has only recently become more commonplace. Aircraft designers have been using composite materials to build lightweight planes for many years and the vast majority of recreational boat hulls are constructed from fiberglass. The Chevrolet Corvette has been constructed with a fiberglass body since it was first introduced in 1953. Although some components had been constructed of composites previously, McLaren raced the first Formula One car constructed with a CF chassis in the early 1980s [18]. The high strength to weight ratio of composite materials allowed the Corvette and McLaren to be much lighter than their competitors, the same reason why composites are being used much more frequently in vehicles today.

With the need to meet ever increasing fuel economy and emissions restrictions, automakers are designing their vehicles to be as light as possible. However, the high costs associated with composite manufacturing prohibit them from being used in every application. As of 2013, extensive use of CF is limited to high end sports cars such as McLaren, Ferrari, Porsche, and Koenigsegg. These manufacturers build some of their cars with CF structural components such as the chassis tub, although the total vehicle cost can exceed $1 million. Some less expensive vehicles use CF as well, but only in limited quantities for specific components in order to keep their total costs down. Typically the use of CF in these vehicles is limited to body panels or decorative trim.

In the modern racing world, Formula One, Indy, and LeMans Prototype cars are constructed almost entirely out of CF and use the material for everything from the steering wheel to sacrificial crash absorbing structures.

2.3 Design

Starting with the generalized 3-D version of Hooke's Law for linear-elastic material

$$\sigma_{ij} = C_{ijkl}\varepsilon_{kl} \qquad \text{where i, j, k, l = 1, 2, 3,} \tag{2.3.1}$$

and taking into account the fact that the stress and strain matrices have symmetry, it is common practice within composites to express the orthotropic constitutive equation in the following form [16].

$$\begin{Bmatrix} \sigma_1 \\ \sigma_2 \\ \sigma_3 \\ \tau_{12} \\ \tau_{31} \\ \tau_{23} \end{Bmatrix} = \begin{bmatrix} C_{11} & C_{12} & C_{13} & 0 & 0 & 0 \\ C_{21} & C_{22} & C_{23} & 0 & 0 & 0 \\ C_{31} & C_{32} & C_{33} & 0 & 0 & 0 \\ 0 & 0 & 0 & C_{44} & 0 & 0 \\ 0 & 0 & 0 & 0 & C_{55} & 0 \\ 0 & 0 & 0 & 0 & 0 & C_{66} \end{bmatrix} \begin{Bmatrix} \varepsilon_1 \\ \varepsilon_2 \\ \varepsilon_3 \\ \gamma_{12} \\ \gamma_{31} \\ \gamma_{23} \end{Bmatrix} \tag{2.3.2}$$

where the subscripts 1, 2, and 3 indicate the coordinate system of the composite material. This equation has taken into account the orthotropic properties of the FRC as evidenced by the uncoupled shear-extension and shear-shear terms. It is also worthwhile to note that the orthotropic stiffness (or elasticity) matrix is symmetric so there are only 9 independent material constants in this equation.

The inverse of the stiffness matrix is the compliance matrix, which is very useful in determining material properties from physical tests. Rewritten in terms of compliance, Equation 2.3.2 becomes [16]

$$\begin{Bmatrix} \varepsilon_1 \\ \varepsilon_2 \\ \varepsilon_3 \\ \gamma_{12} \\ \gamma_{31} \\ \gamma_{23} \end{Bmatrix} = \begin{bmatrix} S_{11} & S_{12} & S_{13} & 0 & 0 & 0 \\ S_{21} & S_{22} & S_{23} & 0 & 0 & 0 \\ S_{31} & S_{32} & S_{33} & 0 & 0 & 0 \\ 0 & 0 & 0 & S_{44} & 0 & 0 \\ 0 & 0 & 0 & 0 & S_{55} & 0 \\ 0 & 0 & 0 & 0 & 0 & S_{66} \end{bmatrix} \begin{Bmatrix} \sigma_1 \\ \sigma_2 \\ \sigma_3 \\ \tau_{12} \\ \tau_{31} \\ \tau_{23} \end{Bmatrix}. \tag{2.3.3}$$

The compliance matrix is defined using three engineering constants: Young's modulus (E), Poisson's ratio (ν), and shear modulus (G). Both the Young's moduli and shear moduli have unique values for each of the three directions, resulting in 6 constants between those two properties ($E_1, E_2, E_3, G_{12}, G_{13}, G_{23}$). Poisson's ratio also has 6 unique values ($v_{12}, v_{13}, v_{23}, v_{21}, v_{31}, v_{32}$). These 12 constants are used to define the compliance matrix as shown below [16].

$$\begin{Bmatrix} \varepsilon_1 \\ \varepsilon_2 \\ \varepsilon_3 \\ \gamma_{12} \\ \gamma_{31} \\ \gamma_{23} \end{Bmatrix} = \begin{bmatrix} \frac{1}{E_1} & -\frac{v_{21}}{E_2} & -\frac{v_{31}}{E_3} & 0 & 0 & 0 \\ -\frac{v_{12}}{E_1} & \frac{1}{E_2} & -\frac{v_{32}}{E_3} & 0 & 0 & 0 \\ -\frac{v_{13}}{E_1} & -\frac{v_{23}}{E_2} & \frac{1}{E_3} & 0 & 0 & 0 \\ 0 & 0 & 0 & \frac{1}{G_{12}} & 0 & 0 \\ 0 & 0 & 0 & 0 & \frac{1}{G_{13}} & 0 \\ 0 & 0 & 0 & 0 & 0 & \frac{1}{G_{23}} \end{bmatrix} \begin{Bmatrix} \sigma_1 \\ \sigma_2 \\ \sigma_3 \\ \tau_{12} \\ \tau_{31} \\ \tau_{23} \end{Bmatrix} \tag{2.3.4}$$

Even though there are a total of 12 unique constants present in the above matrix, there are only 9 independent terms. This is because of the reciprocity relationship that exists with the extension-extension coupling terms, where

$$\frac{v_{12}}{E_1} = \frac{v_{21}}{E_2},\ \frac{v_{13}}{E_1} = \frac{v_{31}}{E_3},\ \frac{v_{23}}{E_2} = \frac{v_{32}}{E_3}\ . \tag{2.3.5}$$

Both the stiffness and compliance matrices are mutually invertible, but the terms in the compliance matrix are simpler and have tangible physical interpretation [16]. However, in the world of FEA, the stiffness matrix is more often used because a displacement is prescribed and the material response is calculated.

The total number of unique constants can be further reduced by assuming the composite is in a state of plane stress. In this case, σ_3, τ_{31}, and τ_{23} are all set to zero and Equation 2.3.4 reduces to

$$\begin{Bmatrix} \varepsilon_1 \\ \varepsilon_2 \\ \gamma_{12} \end{Bmatrix} = \begin{bmatrix} \frac{1}{E_1} & -\frac{v_{21}}{E_2} & 0 \\ -\frac{v_{12}}{E_1} & \frac{1}{E_2} & 0 \\ 0 & 0 & \frac{1}{G_{12}} \end{bmatrix} \begin{Bmatrix} \sigma_1 \\ \sigma_2 \\ \tau_{12} \end{Bmatrix} \tag{2.3.6}$$

Rewriting in terms of stiffness

$$\begin{Bmatrix} \sigma_1 \\ \sigma_2 \\ \tau_{12} \end{Bmatrix} = \frac{1}{1-v_{12}v_{21}} \begin{bmatrix} E_1 & v_{21}E_1 & 0 \\ v_{12}E_2 & E_2 & 0 \\ 0 & 0 & (1-v_{12}v_{21})G_{12} \end{bmatrix} \begin{Bmatrix} \varepsilon_1 \\ \varepsilon_2 \\ \gamma_{12} \end{Bmatrix} \tag{2.3.7}$$

This form of the stiffness matrix is what will be used in the FEA program and will be discussed in greater detail in Chapter 4. For the rest of this chapter, the compliance and stiffness matrices will be referred to as the $[S]$ and $[Q]$ matrices, respectively.

The subscripts 1 and 2 refer to the composite fiber (longitudinal) and matrix (transverse) directions, respectively. In order to translate between these local coordinates and the system global coordinates, several transformation matrices are required.

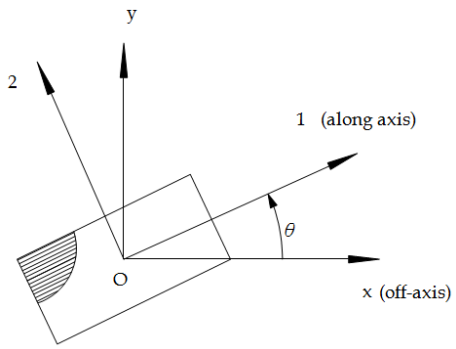

Figure 2. Relationship Between Local and Global Coordinates.

With the local (1,2) and global coordinates (x,y) defined as shown in Figure 1, the stress transformation matrix is [14,16]

$$\begin{Bmatrix}\sigma_1\\ \sigma_2\\ \tau_{12}\end{Bmatrix} = [T_\sigma]\begin{Bmatrix}\sigma_x\\ \sigma_y\\ \tau_{xy}\end{Bmatrix} \tag{2.3.8}$$

where

$$[T_\sigma] = \begin{bmatrix} cos^2\theta & sin^2\theta & 2sin\theta cos\theta \\ sin^2\theta & cos^2\theta & -2sin\theta cos\theta \\ -sin\theta cos\theta & sin\theta cos\theta & cos^2\theta - sin^2\theta \end{bmatrix} \tag{2.3.9}$$

The strain transformation matrix is

$$\begin{Bmatrix}\varepsilon_1\\ \varepsilon_2\\ \gamma_{12}\end{Bmatrix} = [T_\varepsilon]\begin{Bmatrix}\varepsilon_x\\ \varepsilon_y\\ \gamma_{xy}\end{Bmatrix} \tag{2.3.10}$$

where

$$[T_\varepsilon] = \begin{bmatrix} cos^2\theta & sin^2\theta & sin\theta cos\theta \\ sin^2\theta & cos^2\theta & -sin\theta cos\theta \\ -2sin\theta cos\theta & 2sin\theta cos\theta & cos^2\theta - sin^2\theta \end{bmatrix} \tag{2.3.11}$$

Rearranging Equation 2.3.8 and substituting in Equation 2.3.7

$$\begin{Bmatrix}\sigma_x\\ \sigma_y\\ \tau_{xy}\end{Bmatrix} = [T_\sigma]^{-1}[Q]\begin{Bmatrix}\varepsilon_1\\ \varepsilon_2\\ \gamma_{12}\end{Bmatrix} \tag{2.3.12}$$

Now substituting Equation 2.3.10 into 2.3.12 and defining $[\bar{Q}]$ [14, 16]

$$\begin{Bmatrix}\sigma_x\\ \sigma_y\\ \tau_{xy}\end{Bmatrix} = [T_\sigma]^{-1}[Q][T_\varepsilon]\begin{Bmatrix}\varepsilon_x\\ \varepsilon_y\\ \gamma_{xy}\end{Bmatrix} \tag{2.3.13a}$$

$$[\bar{Q}] = [T_\sigma]^{-1}[Q][T_\varepsilon] \tag{2.3.13b}$$

an equation for relating stress and strain in global coordinates is obtained.

$$\begin{Bmatrix}\sigma_x\\ \sigma_y\\ \tau_{xy}\end{Bmatrix} = \begin{bmatrix}\bar{Q}_{11} & \bar{Q}_{12} & \bar{Q}_{16}\\ \bar{Q}_{12} & \bar{Q}_{22} & \bar{Q}_{26}\\ \bar{Q}_{16} & \bar{Q}_{26} & \bar{Q}_{66}\end{bmatrix}\begin{Bmatrix}\varepsilon_x\\ \varepsilon_y\\ \gamma_{xy}\end{Bmatrix} \tag{2.3.14}$$

The $[\bar{Q}]$ matrix includes a messy array of high order sine and cosine terms which makes it difficult to visualize the effects of altering lamina orientation. Tsai and Pagano [17] have rewritten the equations in an invariant form that makes interpretation more straightforward.

$$\begin{aligned}
\bar{Q}_{11} &= U_1 + U_2 cos2\theta + U_3 cos4\theta \\
\bar{Q}_{22} &= U_1 - U_2 cos2\theta + U_3 cos4\theta \\
\bar{Q}_{12} &= U_4 - U_3 cos4\theta \\
\bar{Q}_{16} &= \frac{1}{2} U_2 sin2\theta - U_3 sin4\theta \\
\bar{Q}_{26} &= \frac{1}{2} U_2 sin2\theta - U_3 sin4\theta \\
\bar{Q}_{66} &= U_5 - U_3 cos4\theta
\end{aligned} \tag{2.3.15}$$

Where

$$\begin{aligned}
U_1 &= \frac{3Q_{11}+3Q_{22}+2Q_{12}+4Q_{66}}{8} \\
U_2 &= \frac{Q_{11}-Q_{22}}{2} \\
U_3 &= \frac{Q_{11}+Q_{22}-2Q_{12}-4Q_{66}}{8} \\
U_4 &= \frac{Q_{11}+Q_{22}+6Q_{12}-4Q_{66}}{8} \\
U_5 &= \frac{Q_{11}+Q_{22}-2Q_{12}+4Q_{66}}{8}
\end{aligned} \tag{2.3.16}$$

The inverse of Equation 2.3.14 can be found the same way [14,16].

$$\begin{Bmatrix} \varepsilon_x \\ \varepsilon_y \\ \gamma_{xy} \end{Bmatrix} = [T_\varepsilon]^{-1}[S][T_\sigma] \begin{Bmatrix} \sigma_x \\ \sigma_y \\ \tau_{xy} \end{Bmatrix} \tag{2.3.17a}$$

$$[\bar{S}] = [T_\varepsilon]^{-1}[S][T_\sigma] \tag{2.3.17b}$$

Such that

$$\begin{Bmatrix} \varepsilon_x \\ \varepsilon_y \\ \gamma_{xy} \end{Bmatrix} = \begin{bmatrix} \bar{S}_{11} & \bar{S}_{12} & \bar{S}_{16} \\ \bar{S}_{12} & \bar{S}_{22} & \bar{S}_{26} \\ \bar{S}_{16} & \bar{S}_{26} & \bar{S}_{66} \end{bmatrix} \begin{Bmatrix} \sigma_x \\ \sigma_y \\ \tau_{xy} \end{Bmatrix} \tag{2.3.18}$$

The invariant form of the global compliance matrix is [17]

$$\begin{aligned} \bar{S}_{11} &= V_1 + V_2 cos2\theta + V_3 cos4\theta \\ \bar{S}_{22} &= V_1 - V_2 cos2\theta + V_3 cos4\theta \\ \bar{S}_{12} &= V_4 - V_3 cos4\theta \\ \bar{S}_{16} &= \frac{1}{2} V_2 sin2\theta - V_3 sin4\theta \\ \bar{S}_{26} &= \frac{1}{2} V_2 sin2\theta - V_3 sin4\theta \\ \bar{S}_{66} &= V_5 - V_3 cos4\theta \end{aligned} \tag{2.3.19}$$

where

$$\begin{aligned} V_1 &= \frac{3S_{11}+3S_{22}+2S_{12}+4S_{66}}{8} \\ V_2 &= \frac{S_{11}-S_{22}}{2} \\ V_3 &= \frac{S_{11}+S_{22}-2S_{12}-S_{66}}{8} \\ V_4 &= \frac{S_{11}+S_{22}+6S_{12}-S_{66}}{8} \\ V_5 &= \frac{S_{11}+S_{22}+2S_{12}-S_{66}}{8} \end{aligned} \tag{2.3.20}$$

A composite laminate is created when multiple layers of a composite material are stacked on top of each other and then bonded together. The anisotropic behavior of unidirectional FRCs allows the designer to orient each lamina in a specific direction to obtain a laminate that meets the strength requirements of the part. It also means that the final part will not be orders of magnitude stronger than it needs to be in directions other

than that of the applied load. The equations just presented can be used to determine the response of a composite laminate to a given stress state.

Since the individual laminae are bonded together, it is assumed that adjacent plies do not slip over each other [14,16]. This assumption leads to a linear strain variation across the thickness of the laminate. However, each lamina will have unique stiffness properties due to its orientation relative to the strain direction. The stress at any point in a lamina is a function of the strain at the mid-plane of the laminate, ε^o, the distance of the point from the mid-plane of the laminate, z, and the curvature of the laminate, k [14].

$$\begin{Bmatrix} \sigma_x \\ \sigma_y \\ \tau_{xy} \end{Bmatrix} = \begin{bmatrix} \bar{Q}_{11} & \bar{Q}_{12} & \bar{Q}_{16} \\ \bar{Q}_{12} & \bar{Q}_{22} & \bar{Q}_{26} \\ \bar{Q}_{16} & \bar{Q}_{26} & \bar{Q}_{66} \end{bmatrix}_n \begin{Bmatrix} \varepsilon_x^o \\ \varepsilon_y^o \\ \gamma_{xy}^o \end{Bmatrix} + z \begin{bmatrix} \bar{Q}_{11} & \bar{Q}_{12} & \bar{Q}_{16} \\ \bar{Q}_{12} & \bar{Q}_{22} & \bar{Q}_{26} \\ \bar{Q}_{16} & \bar{Q}_{26} & \bar{Q}_{66} \end{bmatrix}_n \begin{Bmatrix} k_x \\ k_y \\ k_{xy} \end{Bmatrix} \tag{2.3.21}$$

Each lamina has its own stiffness matrix, $[\bar{Q}]$, depending on the orientation angle. The lamina stiffness matrix does not vary across the lamina; therefore the stress varies linearly across each lamina as a function of the strain across the lamina. Figure 3 shows how strain and stress can vary across a laminate with curvature.

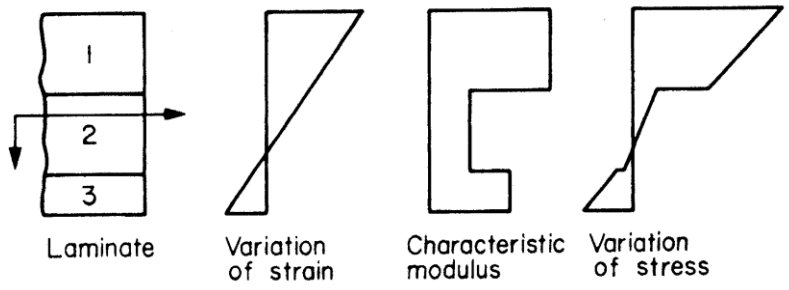

Figure 3. Variations of Stress and Strain Within a Laminate [14].

Even though the stress varies linearly across each lamina, it is possible for a stress discontinuity to be present at the interface between two plies with different stiffness matrices. When this occurs, the stress gradients are also different. If the laminate does not

experience any curvature, the strain will be constant across the entire laminate. The stress can still vary from lamina to lamina, but it will be constant across each individual one.

2.4 Composite Failure

The previous section discussed how to calculate the stress experienced by each individual lamina in a composite laminate. Figure 3 also shows how stress might vary across the thickness of a laminate. Because of this variation in stress, each lamina will fail at a different load. The stress values are what determine the failure point of each lamina within the laminate, and then the failure point of the laminate as a whole. Depending on lamina orientation, failure can occur either in the fiber or in the matrix. It is expected that plies will fail starting with the weakest in the load direction. This first ply failure (FPF) may not even have an effect on the laminate if the strength contribution of the failed lamina was relatively insignificant to begin with. Subsequent lamina failures will degrade the stiffness of the laminate according to their individual contributions. It is still possible for the laminate to withstand more load after plies have failed, but it will do so with larger deflections than it would have previously.

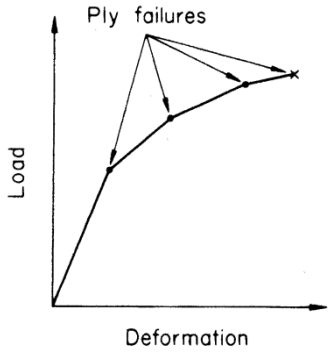

Figure 4. Laminate Load-Deformation Curve with Laminated Ply Failures [14].

A third mode of composite failure (after fiber and matrix failure) is delamination between plies. One of the basic assumptions of laminated plate theory is that there is perfect adhesion (no slip) between plies in a laminate. This allows for the linear strain variation

across the entire laminate, but as the differences between ply stresses increases and failure starts to occur, this assumption quickly breaks down.

The final type of composite laminate failure is material buckling. Buckling can occur at any load higher than the critical load, which for a perfectly straight and centrally loaded column is defined as [18]

$$P_{cr} = \frac{\pi^2 EI}{4l^2} \tag{2.4.1}$$

Buckling can be avoided by designing the part with an appropriate aspect ratio of diameter to length. Local buckling, where the material begins to fold over itself, may still occur and is typically more difficult to predict.

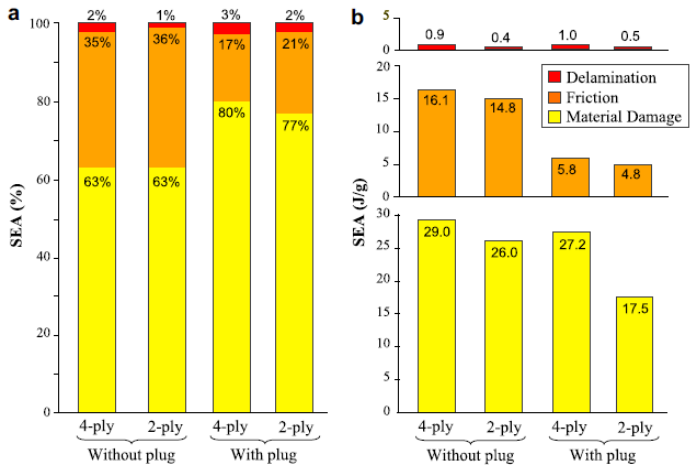

Figure 5. Contribution of Failure Modes to SEA in (a) Percent and (b) Absolute Energy Absorbed [18].

It is a combination of all of the failure modes discussed, in addition to friction generated at the contact surface, which determines the total amount of energy absorbed. Figure 5 shows the contributions of delamination, friction at the contact surface, and the remaining failure modes to the total Specific Energy Absorbed (SEA), where

$$SEA = \frac{Total\ Energy\ Absorbed}{Mass\ of\ Crushed\ Material}. \tag{2.4.2}$$

Two versions of the test are shown: one with an extruded boss (plug) on the crushing plate to force all of the material away from the center of the tube, and one without.

Chapter 3. Finite Element Modeling

3.1 Overview

The basic premise behind finite element (FE) modeling revolves around dividing a single part into multiple sections and performing load balancing calculations on each section. These "local" equations generated from each section are then combined to form "global" mass, damping, and stiffness matrices which are applied to the entire part to determine its response. Equation 3.1.1 shows these global matrices assembled with the displacement (u), velocity ($\dot{u}$), acceleration ($\ddot{u}$), and force ($f(t)$) vectors.

$$[M]\{\ddot{u}\} + [C]\{\dot{u}\} + [K]\{u\} = \{f(t)\} \tag{3.1.1}$$

FE modeling has a wide variety of applications ranging from simple static load bearing analyses all the way to assemblies undergoing nonlinear deformations.

3.2 Techniques

With any FE simulation it is important to first determine how to analyze the system before attempting to build the model. Different analysis processes can yield very different results even if all other parameters such as loading and boundary conditions are kept the same.

3.2.1 Linear vs. Non-linear

The material response is the most obvious factor in deciding between linear or non-linear analysis. If the response is expected to remain in the linear-elastic region, then a linear analysis is adequate. In this case, the only material properties required for an isotropic material model are the Young's Modulus (E) and Poisson's Ratio (v). However, if the analysis predicts that the material will be stressed past its yield point, the program will simply continue treating the material as if it was still in the linear-elastic region. The

response for this situation is shown by the red dashed line in Figure 6. In order to accurately model the material response past the yield point it is necessary to use a non-linear analysis.

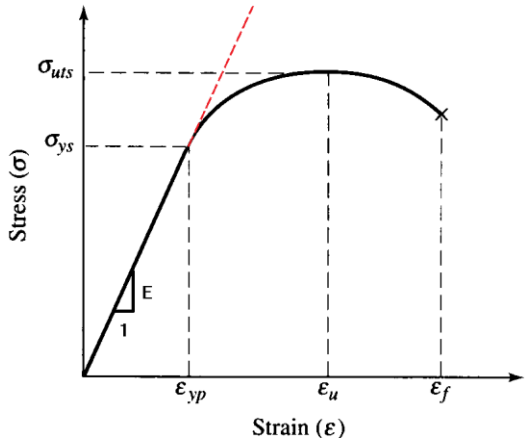

Figure 6. Stress-strain response of a ductile material.

If the material to be modeled has a non-linear elastic region, is expected to be stressed past its yield point, is subject to contact or friction forces, or is expected to buckle, then a non-linear analysis is required. Non-linear analysis also offers the capability to account for plastic deformation and damage growth within the model. Most real world problems are non-linear, so any linear model used to predict a response is only an approximation. Whether a linear approximation is accurate enough is up to the engineer performing the analysis.

The way that Abaqus analyzes a non-linear system is by using the Newton-Raphson method [19]. Two different versions of the method will be discussed here: the standard Newton-Raphson method and the modified Newton-Raphson method. Both methods start by dividing the total load into a number of load increments and calculating an approximate linear response over each iteration within the increment, but they differ in how they calculate that response. The standard method calculates the response to the load increment $\{P\}_n$ based on the tangent stiffness matrix from the previous iteration,

$[K_t(\{u\}_{i-1})]$. Figure 7 shows how the stiffness used for each iteration changes based on the material properties at that point. After calculating the stiffness matrix and load error from the previous iteration, the new displacement is calculated.

$$\{e\}_{i-1} = \{P\}_n - \{r\}_{i-1} \tag{3.2.1}$$

$$\{u\}_i = \{u\}_{i-1} + [K_t(\{u\}_{i-1})]^{-1}\{e\}_{i-1} \tag{3.2.2}$$

Using the new displacement, the new predicted load is calculated and then compared to the load of that increment to obtain the current iteration load error.

$$\{r\}_i = [K(\{u\}_i)]\{u\}_i \tag{3.2.3}$$

$$\{e\}_i = \{P\}_n - \{r\}_i \tag{3.2.4}$$

If the error is within a specified tolerance, the process is repeated for the next load increment. If it is larger than the tolerance, then a new tangent stiffness matrix is calculated based on the end point of the previous iteration and another displacement iteration is calculated for the same load increment.

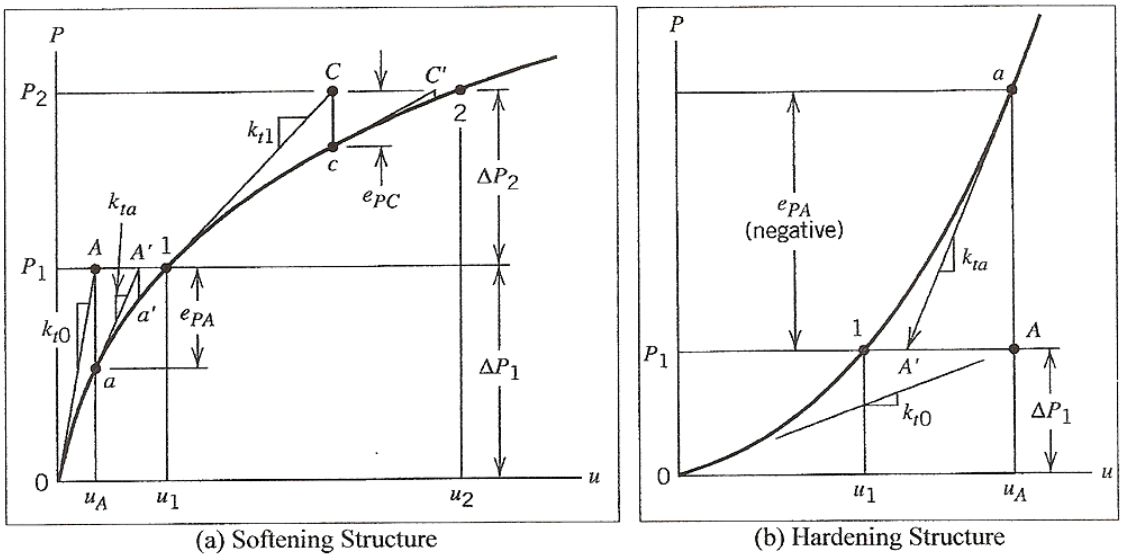

Figure 7. Iterative Process for Newton-Raphson Method [20].

The main advantage to using the standard Newton-Raphson method is that adjusting the stiffness for each iteration allows the increment to converge with fewer

iterations. This gives the method a quadratic convergence rate, so long as the increments are kept small enough [19]. However, the process is computationally expensive due to this same reason; the program must calculate a new stiffness matrix for every single iteration.

A slight modification to the Newton-Raphson method uses the stiffness matrix from the beginning of the increment for every iteration within that increment. By doing this, the need to calculate a new stiffness matrix for every single iteration is eliminated. The downside to this method is that more iterations are required for the increment to converge, as shown in Figure 8. But since those iterations occur more rapidly, the total computation requirement can still be reduced compared to the standard Newton-Raphson method [19].

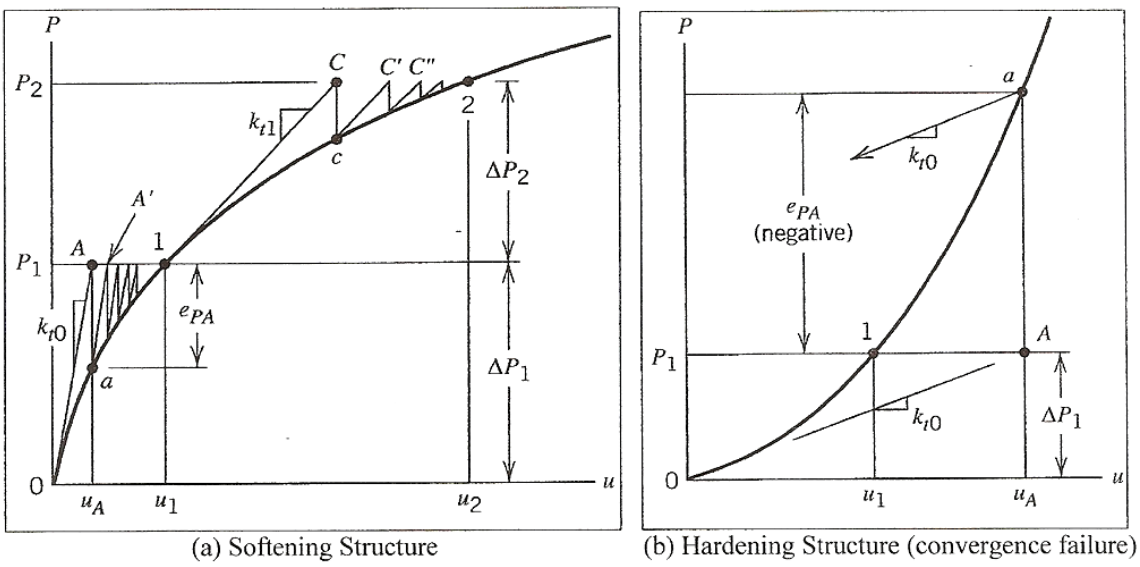

Figure 8. Iterative Process for Modified Newton-Raphson Method [20].

Another limitation to the modified Newton-Raphson method is that since it is less fluid in the evolution of the stiffness matrix, it is best suited for only mildly non-linear problems [19]. By default, Abaqus uses the standard Newton-Raphson method.

3.2.2 Static vs. Dynamic

The basic difference between static and dynamic analyses is how the forces are balanced in the system. In a static problem, the load is divided into increments and $\sum F = 0$ at the end of each increment. The analysis runs until the total load has been applied. The external forces applied to a part must be balanced solely by internal forces from deformations. The best candidates for static analysis are steady state or quasi-static problems where the applied load does not change over time and inertia effects can be neglected.

If there are any time dependent terms that need to be modeled then a dynamic analysis is required. In a dynamic problem, the total simulation time is set by the user then divided into increments. $\sum F = m\ddot{u}$ at the end of each time step. Whereas a static analysis balances external forces with deformations only, a dynamic analysis also includes inertia effects. The analysis will run until the specified time has elapsed, even if a load has not been fully applied or objects are still in motion. Examples of dynamic analyses include vibration analysis, impact, and systems with moving parts.

3.2.3 Implicit vs. Explicit

There are two methods available for integrating a FE model: implicit and explicit integration. The main difference between these two types of integration revolves around the solution process. Implicit integration requires the standard Newton-Raphson method where the value of the tangent stiffness matrix goes through multiple iterations until the result converges. Explicit integration can solve for the terms in the next increment without the need for any iteration.

3.2.3a Implicit Integration

Implicit integration begins with Newmark's numerical method:

$$\{\dot{u}\}_{n+1} = \{\dot{u}\}_n + \Delta t\{\gamma\{\ddot{u}\}_{n+1} + (1-\gamma)\{\ddot{u}\}_n\} \tag{3.2.5}$$

$$\{u\}_{n+1} = \{u\}_n + \Delta t\{\dot{u}\}_n + (\Delta t)^2\left\{\left(\tfrac{1}{2}-\beta\right)\{\ddot{u}\}_n + \beta\{\ddot{u}\}_{n+1}\right\} \tag{3.2.6}$$

$$\gamma = \tfrac{1}{2} - \alpha \quad , \; \beta = \tfrac{1}{4}(1-\alpha)^2 \quad , \quad -\tfrac{1}{3} \le \alpha \le 0$$

The value of α determines the amount of numerical damping introduced during the analysis [19].

Rearranging 3.2.6 to solve for $\{\ddot{u}\}_{n+1}$

$$\{\ddot{u}\}_{n+1} = \tfrac{1}{\beta(\Delta t)^2}\{\{u\}_{n+1} - \{u\}_n - \Delta t\{\dot{u}\}_n\} - \left(\tfrac{1}{2\beta} - 1\right)\{\ddot{u}\}_n \tag{3.2.7}$$

Substituting 3.2.7 into 3.2.5 and simplifying

$$\{\dot{u}\}_{n+1} = \tfrac{\gamma}{\beta\Delta t}\{\{u\}_{n+1} - \{u\}_n\} + (1-\tfrac{\gamma}{\beta})\{\dot{u}\}_n + \Delta t\left(1 - \tfrac{\gamma}{2\beta}\right)\{\ddot{u}\}_n \tag{3.2.8}$$

From Equation 3.1.1

$$[M]\{\ddot{u}\}_{n+1} + [C]\{\dot{u}\}_{n+1} + [K]\{u\}_{n+1} = \{f\}_{n+1} \tag{3.2.9}$$

Substituting 3.2.7 and 3.2.8 in for $\{\ddot{u}\}_{n+1}$ and $\{\dot{u}\}_{n+1}$, respectively, and solving for $\{u\}_{n+1}$ terms on the left:

$$[K]_{eff}\{u\}_{n+1} = \{f\}_{eff} \tag{3.2.10a}$$

where

$$[K]_{eff} = \left[\tfrac{1}{\beta(\Delta t)^2}[M] + \tfrac{\gamma}{\beta\Delta t}[C] + [K]\right] \tag{3.2.10b}$$

and

$$\begin{aligned}\{f\}_{eff} = \{f\}_{n+1} &+ [M]\left\{\tfrac{1}{\beta(\Delta t)^2}\{u\}_n + \tfrac{1}{\beta\Delta t}\{\dot{u}\}_n + \left(\tfrac{1}{2\beta} - 1\right)\{\ddot{u}\}_n\right\} \\ &+ [C]\left\{\tfrac{\gamma}{\beta\Delta t}\{u\}_n + \left(\tfrac{\gamma}{\beta} - 1\right)\{\dot{u}\}_n + \Delta t\left(\tfrac{\gamma}{2\beta} - 1\right)\{\ddot{u}\}_n\right\}\end{aligned} \tag{3.2.10c}$$

Finally, solving for displacement at the next increment

$$\{u\}_{n+1} = [K]_{eff}^{-1}\{f\}_{eff} \tag{3.2.11}$$

When written in this form, equation 3.2.11 shows the simplicity of the FE method. At its core, FEA is simply solving for displacement using an effective force and stiffness. By simultaneously solving for the displacement in every direction at every node, the total system response can be determined. Equation 3.2.11 also gives insight as to why the implicit method can be computationally expensive. The inversion of the K_{eff} matrix requires more computation power than the other steps in the implicit process because it is a very large (ndof x ndof) non-diagonal sparse matrix. The other solution method, explicit analysis, greatly reduces computation requirements by only requiring the inversion of a diagonal matrix.

3.2.3b Explicit Integration

Abaqus Explicit uses a form of the central difference method which assumes linear changes in one increment to predict parameters in another increment [19]. Starting with the acceleration $\{\ddot{u}\}$ at increment n, using central difference integration:

$$\{\ddot{u}\}_n = \frac{\{\dot{u}\}_{n+1/2} - \{\dot{u}\}_{n-1/2}}{\Delta t} \tag{3.2.12}$$

Equation 3.2.12 defines acceleration in the nth increment using velocity at the next half-increment ($\dot{u}_{n+1/2}$), velocity at the previous half-increment ($\dot{u}_{n-1/2}$), and the elapsed time between the two (Δt). The central difference method can also be applied to half-increments as shown in Equations 3.2.13.

$$\{\dot{u}\}_{n+1/2} = \frac{\{u\}_{n+1} - \{u\}_n}{\Delta t} \tag{3.2.13a}$$

$$\{\dot{u}\}_{n-1/2} = \frac{\{u\}_n - \{u\}_{n-1}}{\Delta t} \tag{3.2.13b}$$

Substituting Equations 3.2.13 into 3.2.12 gives the acceleration in terms of displacements.

$$\{\ddot{u}\}_n = \frac{1}{\Delta t}\left\{\frac{\{u\}_{n+1}-\{u\}_n}{\Delta t} - \frac{\{u\}_n-\{u\}_{n-1}}{\Delta t}\right\} \tag{3.2.14}$$

Rearranging…

$$\{\ddot{u}\}_n = \frac{1}{(\Delta t)^2}\{\{u\}_{n+1} - 2\{u\}_n + \{u\}_{n-1}\} \tag{3.2.15}$$

By applying the central difference method, an expression for velocity can be obtained in terms of whole-increment steps of displacement.

$$\{\dot{u}\}_n = \frac{\{u\}_{n+1}-\{u\}_{n-1}}{2\Delta t} \tag{3.2.16}$$

Substituting Equations 3.2.15 and 3.2.16 into 3.1.1:

$$\frac{[M]}{(\Delta t)^2}\{\{u\}_{n+1} - 2\{u\}_n + \{u\}_{n-1}\} + \frac{[C]}{2\Delta t}\{\{u\}_{n+1} - \{u\}_{n-1}\} + [K]\{u\}_n = \{f\}_n \tag{3.2.17}$$

Rearranging to separate each increment:

$$\left[\frac{[M]}{(\Delta t)^2} + \frac{[C]}{2\Delta t}\right]\{u\}_{n+1} + \left[[K] - \frac{2[M]}{(\Delta t)^2}\right]\{u\}_n + \left[\frac{[M]}{(\Delta t)^2} - \frac{[C]}{2\Delta t}\right]\{u\}_{n-1} = \{f\}_n \tag{3.2.18}$$

Solving for displacement at the next increment:

$$\{u\}_{n+1} = \left[\frac{[M]}{(\Delta t)^2} + \frac{[C]}{2\Delta t}\right]^{-1}\left\{\{f\}_n - \left[[K] - \frac{2[M]}{(\Delta t)^2}\right]\{u\}_n - \left[\frac{[M]}{(\Delta t)^2} - \frac{[C]}{2\Delta t}\right]\{u\}_{n-1}\right\} \tag{3.2.19}$$

By using Equations 3.2.13a and 3.2.19 to solve for the velocity at the next half increment and displacement at the next increment, respectively, this process is considered explicit because the state of the element can be advanced using known values at the current and previous increments [19].

A slightly different form of the central difference method is used by Abaqus. Rearranging Equation 3.2.12 to solve for the next half increment gives:

$$\{\dot{u}\}_{n+1/2} = \{\dot{u}\}_{n-1/2} + \frac{\Delta t_{n+1}+\Delta t_n}{2}\{\ddot{u}\}_n \tag{3.2.20}$$

This equation assumes the time step is not constant and therefore uses an average. Likewise, Equation 3.2.13a can be rearranged to solve for displacement at the next increment:

$$\{u\}_{n+1} = \{u\}_n + \Delta t_{n+1}\{\dot{u}\}_{n+1/2} \tag{3.2.21}$$

Since all the terms present in this equation reside in the same time step, no average is necessary. Abaqus uses Equations 3.2.20 and 3.2.21 to solve for the displacement and velocity, but the acceleration term in 3.2.20 still needs to be solved. Just like the previous method, Equation 3.1.1 is used. Rearranging to solve for acceleration:

$$\{\ddot{u}\}_n = [M]^{-1}\{\{f\}_n - [C]\{\dot{u}\}_n - [K]\{u\}_n\} \tag{3.2.22}$$

There is still one minor issue with this method so far: it is not self-starting. When calculating the very first term at n=0, $\{\dot{u}\}_{1/2}$, no value exists for $\{\dot{u}\}_{-1/2}$ in Equation 3.2.20. To remedy this, a half-step forward difference technique is implemented.

$$\{\dot{u}\}_{1/2} = \{\dot{u}\}_0 + \frac{\Delta t_0}{2}\{\ddot{u}\}_0 \tag{3.2.23}$$

An expression for $\{\dot{u}\}_{-1/2}$ can then be obtained by substituting Equation 3.2.23 into 3.2.20.

$$\{\dot{u}\}_{-1/2} = \{\dot{u}\}_0 - \frac{\Delta t_0}{2}\{\ddot{u}\}_0 \tag{3.2.24}$$

Equation 3.2.24 is solved once at the beginning of the analysis just to start the process.

One advantage of using an explicit process over an implicit process is that since all of the required terms are already known, there is no need to guess a term from the next increment and iterate until the result converges. However, the significant increase in computational efficiency comes from using the diagonal (lumped) element mass and damping matrices [19]. Inverting the resulting diagonal matrix requires significantly less computational power than inverting the stiffness matrix as is done in implicit routines.

Since the central difference method assumes a linear change in the state of the element from one increment to the next, small time steps are required in order for the method to be stable. The necessary time step required for an explicit analysis to be stable is orders of magnitude smaller than the time step possible with an implicit method [19]. This makes explicit analysis best suited for impact or short duration dynamic analysis. The size of the time step required for stability depends largely on the density of the material and size of the elements in the model. Within Abaqus, largest stable time step is defined in terms of the highest eigenvalue in the system (ω_{max}) and a damping coefficient (ξ) added in to control high frequency oscillations [19].

$$\Delta t \leq \frac{2}{\omega_{max}} \left(\sqrt{1+\xi^2} - \xi\right) \tag{3.2.25}$$

The use of the highest eigenvalue of the system to calculate the stable range for the time step has a physical interpretation as well. By calculating the time step in this way, Abaqus sets the maximum time step "approximately equal to the time for an elastic wave to cross the smallest element dimension in the model" [19]. Abaqus will calculate the time step automatically without the need for user input and then either adjust it after each increment or keep it constant, depending on which method the user specified.

Chapter 4. FE Modeling of Composite Materials Using Abaqus

4.1 Overview

There are several different ways to implement composite material properties into Abaqus. The most straightforward of these involves building the part out of shell elements, defining a section with the appropriate layup, and then applying that section to the part. Shell elements are well suited for modeling composite layups because they share a common assumption: all stress is in-plane. While real-world applications may experience some out of plane stress, that stress is low enough relative to the in-plane stress that the assumption remains an accurate approximation.

Defining material properties for a composite lamina is as simple as defining properties for any other material. However, instead of defining only one elastic stiffness value, two are required (one for each direction) along with the three shear moduli associated with the three material planes. For the purpose of this analysis, all three values of the shear modulus were set equal to the in-plane modulus. The property module is also where all of the material damage parameters are defined.

Once the composite lamina properties are defined they can be used to create a layup complete with ply thickness, stack orientation, and number of integration points per ply. The local coordinate system of the part must be defined in order to ensure that the laminae are correctly oriented.

4.2 Damage Initiation

Damage initiation is simply the point at which the material properties are first affected. How the material behaves after damage has been initiated is determined by the

damage evolution criteria. Four damage initiation variables (F_{FT}, F_{FC}, F_{MT}, and F_{MC}) are used to determine when an element has been stressed sufficiently to cause damage. These variables start out with a value of 0 and increase according to set criteria until they reach a value of 1.0. Once one of the damage initiation variables reach a value of 1.0, damage has occurred in that direction for that element. When the damage evolution model is active, element stiffness is not affected at all until the damage initiation variable has reached 1.0. Without the damage evolution model active, Abaqus will simply keep track of the damage initiation variables without adjusting the strength of the element to account for damage.

4.2.1 Hashin Damage Criteria

Abaqus has two built in damage initiation criteria to predict when damage has occurred in an element. Both models separate the failure criteria into two primary failure modes: fiber failure and matrix failure. Fiber failure consists of fibers either rupturing in tension or bucking in compression, while matrix failure is when cracks form in the matrix parallel to the fiber direction. The models then subdivide each of those primary failure modes into two more modes for a total of four individual failure modes: fiber tension, fiber compression, matrix tension, and matrix compression [21,22]. The actual physical damage is not modeled within Abaqus, just the effects of the damage on the strength of the laminate in each of the four modes.

Fiber Tension ($\hat{\sigma}_{11} \geq 0$)

$$F_{FT} = \left(\frac{\hat{\sigma}_{11}}{S_{FT}}\right)^2 + \alpha\left(\frac{\hat{\sigma}_{12}}{\tau_F}\right)^2 , \ \ where\ 0 \leq \alpha \leq 1 \tag{4.2.1}$$

Fiber Compression ($\hat{\sigma}_{11} < 0$)

$$F_{FC} = \left(\frac{\hat{\sigma}_{11}}{S_{FC}}\right)^2 \tag{4.2.2}$$

Matrix Tension ($\hat{\sigma}_{22} \geq 0$)

$$F_{MT} = \left(\frac{\hat{\sigma}_{22}}{S_{MT}}\right)^2 + \left(\frac{\hat{\sigma}_{12}}{\tau_F}\right)^2 \tag{4.2.3}$$

Matrix Compression ($\hat{\sigma}_{22} < 0$)

$$F_{MC} = \left(\frac{\hat{\sigma}_{22}}{2\tau_M}\right)^2 + \left(\left(\frac{S_{MC}}{2\tau_M}\right)^2 - 1\right)\frac{\hat{\sigma}_{22}}{S_{MC}} + \left(\frac{\hat{\sigma}_{12}}{\tau_F}\right)^2 \tag{4.2.4}$$

The effective stress values used in the Hashin criteria are calculated based on the amount of damage present in the material.

Effective Stress, $\{\hat{\sigma}\}$

$$\begin{Bmatrix} \hat{\sigma}_{11} \\ \hat{\sigma}_{22} \\ \hat{\sigma}_{12} \end{Bmatrix} = [M] \begin{Bmatrix} \sigma_{11} \\ \sigma_{22} \\ \sigma_{12} \end{Bmatrix} \tag{4.2.5}$$

where $\{\sigma\}$ is the nominal stress vector and $[M]$ is the damage matrix:

$$[M] = \begin{bmatrix} \frac{1}{(1-d_f)} & 0 & 0 \\ 0 & \frac{1}{(1-d_m)} & 0 \\ 0 & 0 & \frac{1}{(1-d_s)} \end{bmatrix} \tag{4.2.6}$$

Before damage is initiated, $d_f = d_m = d_s = 0$ and M is simply a 3x3 identity matrix. The damage matrix does not play a role in determining the first failure because all the damage variables are still zero since no damage has occurred yet. Where the damage matrix becomes important, though, is in the influence of a failure in one direction on subsequent failure in the other directions. One of the simplest physical examples of this is matrix cracking. If the matrix cracks due to compression, it can no longer carry as much shear load. Its strength is affected in the shear direction even though there may not have been any direct shear loading to degrade it.

The first model, proposed by Hashin and Rotem in 1973 [21], is selected by setting $\alpha = 0$ in the fiber tension mode and $\tau_M = \frac{S_{MC}}{2}$ in the matrix compression mode. This model was developed based around a unidirectional FRC undergoing oscillatory plane stress. The second model was proposed by Hashin in 1980 [22] and requires $\alpha = 1$ in the fiber tension mode. This allows the model to account for the contribution of shear stress to the fiber tensile initiation criterion, as well as including the effects of the matrix compressive strength on the matrix compressive initiation criterion [23]. Both failure criteria will be modeled and the results compared.

4.3 Damage Evolution

Abaqus tracks damage evolution by calculating equivalent stresses and strains in an element. A characteristic length is introduced to the displacement term as a way to normalize the value between different size elements. This characteristic length is then divided out when calculating the equivalent stress so that the equivalent stress is simply the stress in the element. The equivalent displacement values are then used to calculate a damage variable which degrades the strength and stiffness of the damaged element. While the criteria used to determine the onset of damage is stress-based, the damage growth model is strain-based.

Fiber Tension ($\hat{\sigma}_{11} \geq 0, \varepsilon_{11} \geq 0$)

$$\delta_{eq}^{ft} = L^c \sqrt{\langle \varepsilon_{11} \rangle^2 + \alpha {\varepsilon_{12}}^2} \tag{4.3.1a}$$

$$\sigma_{eq}^{ft} = \frac{\langle \sigma_{11} \rangle \langle \varepsilon_{11} \rangle + \alpha \tau_{12} \varepsilon_{12}}{\delta_{eq}^{ft} / L^c} \tag{4.3.1b}$$

Fiber Compression ($\hat{\sigma}_{11} < 0, \varepsilon_{11} < 0$)

$$\delta_{eq}^{fc} = L^c\langle -\varepsilon_{11}\rangle \tag{4.3.2a}$$

$$\sigma_{eq}^{fc} = \frac{\langle -\sigma_{11}\rangle\langle -\varepsilon_{11}\rangle + \langle -\sigma_{11}\rangle}{\delta_{eq}^{fc}/_{L^c}} \tag{4.3.2b}$$

Matrix Tension ($\hat{\sigma}_{22} \geq 0, \varepsilon_{22} \geq 0$)

$$\delta_{eq}^{mt} = L^c\sqrt{\langle \varepsilon_{22}\rangle^2 + {\varepsilon_{12}}^2} \tag{4.3.3a}$$

$$\sigma_{eq}^{mt} = \frac{\langle \sigma_{22}\rangle\langle \varepsilon_{22}\rangle + \tau_{12}\varepsilon_{12}}{\delta_{eq}^{mt}/_{L^c}} \tag{4.3.3b}$$

Matrix Compression ($\hat{\sigma}_{22} < 0, \varepsilon_{22} < 0$)

$$\delta_{eq}^{mc} = L^c\sqrt{\langle -\varepsilon_{22}\rangle^2 + {\varepsilon_{12}}^2} \tag{4.3.4a}$$

$$\sigma_{eq}^{mc} = \frac{\langle -\sigma_{22}\rangle\langle -\varepsilon_{22}\rangle + \tau_{12}\varepsilon_{12}}{\delta_{eq}^{mc}/_{L^c}} \tag{4.3.4b}$$

Where the $\langle \quad \rangle$ represents the Macaulay bracket operator, defined as

$$\langle x\rangle = \frac{(x + |x|)}{2} \tag{4.3.5}$$

so that the equivalent displacement and stress are calculated appropriately for each condition [23]. By using this operator and paying close attention to the sign on each variable, Abaqus ensures that the equivalent stress and displacement for each mode is tracked individually, i.e. a tensile strain in the matrix will not affect the matrix compressive equivalent displacement.

The equivalent displacements are then used to calculate the damage variables which track the cumulative effect of damage on the element. The first four variables (d_f^t, d_f^c, d_m^t, and d_m^c) are calculated directly from equation 4.3.6. There are four unique sets of

δ_{eq}^{o}, δ_{eq}^{F}, and δ_{eq} for each of the four damage modes so that each mode has its own damage variable.

$$d = \frac{\delta_{eq}^{F}(\delta_{eq} - \delta_{eq}^{o})}{\delta_{eq}(\delta_{eq}^{F} - \delta_{eq}^{o})} \tag{4.3.6}$$

with δ_{eq}^{o} being the equivalent displacement at first yield and δ_{eq}^{F} being the equivalent displacement at failure. The shear damage variable, d_s, is determined by the fiber and matrix damages.

$$d_s = 1 - \left(1 - d_f^t\right)\left(1 - d_f^c\right)(1 - d_m^t)(1 - d_m^c) \tag{4.3.7}$$

In the range $\delta_{eq}^{o} \leq \delta_{eq} \leq \delta_{eq}^{F}$, Equation 4.3.6 defines the damage variable as being bounded by $0 \leq d \leq 1$. Before any damage occurs, the equation is not active and $d = 0$. Once the damage variable reaches d_{max} in either the tensile or compressive direction, Abaqus/Explicit will treat that point as if it failed. The upper limit of the damage variable, d_{max}, can be set within Abaqus to a value less than the default value of 1. The same value of d_{max} is used for all damage variables. After all of the integration points of an element have reached d_{max}, Abaqus will delete the element and completely remove its stiffness from the simulation [23].

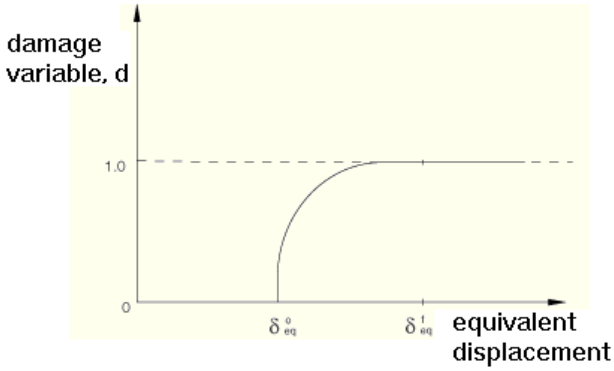

Figure 9. Damage Variable as a Function of Equivalent Displacement [23].

Using the method implemented by Abaqus allows all 5 damage conditions (fiber T/C, matrix T/C, shear) to be calculated using 4 properties which can be obtained from simple material tests. These properties are the total energies dissipated during damage, G^c, in the fiber tension, fiber compression, matrix tension, and matrix compression directions [23]. Figure 10 shows the general response for a material being damaged as modeled in Abaqus.

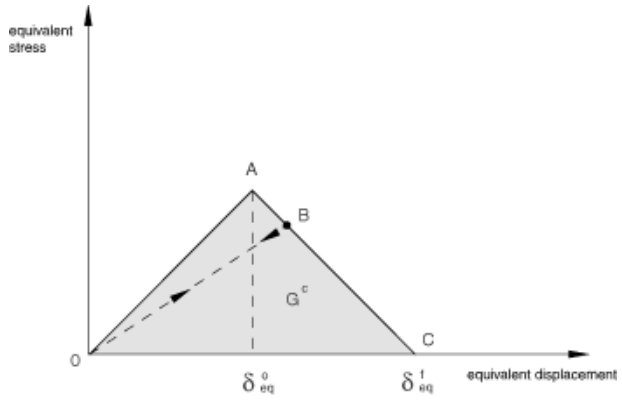

Figure 10. Linear Damage Evolution [23].

As the material is loaded, the response is initially linear-elastic as shown from point O to point A. Once the damage criterion has been satisfied and damage has occurred, Abaqus models the strength degradation of the material as linear softening [23]. If the material were to be unloaded then reloaded after being damaged it would follow the path between point B and point O. As damage within the element grows, point B moves towards point C and both the stiffness and strength of the element decrease. The damage variables are calculated in such a way that the response follows this linear path to δ_{eq}^{F}. The total energy dissipated during damage, G^c, is the area underneath the curve. For brittle materials experiencing catastrophic failure, such as carbon fiber, the line from A to C would be nearly vertical.

The material response while undergoing damage is calculated from the following equation [23].

$$\{\sigma\} = [C_d]\{\varepsilon\} \tag{4.3.8}$$

C_d is the damaged elasticity matrix as defined in Equations 4.3.9.

$$[C_d] = \frac{1}{D}\begin{bmatrix} (1-d_f)E_1 & (1-d_f)(1-d_m)v_{21}E_1 & 0 \\ (1-d_f)(1-d_m)v_{12}E_2 & (1-d_m)E_2 & 0 \\ 0 & 0 & (1-d_s)G_{12}D \end{bmatrix} \tag{4.3.9a}$$

$$D = 1 - (1-d_f)(1-d_m)v_{12}v_{21} \tag{4.3.9b}$$

Equations 4.3.9 show how the stiffness of the material decreases as the values of the damage variables increase. Once a damage variable for an integration point reaches a value of 1, that point no longer contributes any strength or stiffness to the model. Matzenmiller, et al. [24] point out that the normal stress contributions, induced by Poisson's ratio, are the first to be diminished in that they are affected by both damage variables.

4.4 Damage Stabilization

Sometimes Abaqus Standard can have difficulties converging when modeling damage growth with an implicit method [25]. To help with convergence, Abaqus has a viscous regularization scheme which can be utilized. Four properties are required for the viscous regularization to be active. These are viscous coefficients for each of the four failure modes. In Abaqus Explicit, viscous regularization can be used to model rate-dependant material behavior. It slows down the rate of damage growth and increases the fracture energy as deformation rates increase [23].

Chapter 5. Axial Crushing of a Composite Tube

5.1 Physical Test

All of the physical testing and results used in this paper come from experiments performed by Huang and Wang [2] with the purpose of investigating the axial crushing response of composite tubes. Tubular sections with the dimensions shown in Table 2 and lamina properties shown in Table 3 were constructed. Three tubes consisting of 14 plies of unidirectional CF each were laid up to be crushed axially in quasi-static tests.

Table 2. Composite Tube Details [2].

Specimen	Inside Diameter (mm)	Outside Diameter (mm)	Height (mm)	Ply Orientation	Bevel Trigger
B-0	50.00	53.70	100	$[\pm 45/90/0_2/90/0]_s$	No
B-1	50.00	53.68	100	$[\pm 45/90/0_2/90/0]_s$	Yes
B-2	50.00	53.64	100	$[\pm 45/90/0_2/90/0]_s$	Yes

The first tube, B-0, was constructed with full wall thickness along the entire length of the tube. The other tubes, B-1 and B-2, received a 45° bevel on one end in order to control the initiation of crushing. All three tubes had identical layups, inner diameters, and lengths. The slight differences in outer diameters can be attributed to manufacturing process, although the results show that the differences had negligible effect on the performance of the tubes.

Table 3. Material Properties of T700/QY8911 Unidirectional Prepreg [2].

Property	Value
Fiber Volume Ratio (V_f)	.643
Density (ρ)	1.53 g/cm^3
Longitudinal Young's Modulus (E_1)	135 GPa
Transverse Young's Modulus (E_2)	9.12 GPa
In-Plane Shear Modulus (G_{12})	5.67 GPa
Major Poisson's Ratio (ν_{12})	.311
Minor Poisson's Ratio (ν_{21})	.021
Longitudinal Tensile Strength (S_{FT})	2326 MPa
Longitudinal Compressive Strength (S_{FC})	1236 MPa
Transverse Tensile Strength (S_{MT})	51 MPa
Transverse Compressive Strength (S_{MC})	209 MPa
In-Plane Shear Strength (τ_{12})	87.9 MPa
Interlaminar Shear Strength (τ_3)	99.2 MPa

The tubes were each placed between two flat, parallel rigid plates and subjected to quasi-static loading at room temperature. The tests were conducted one tube at a time with a crosshead rate of 2mm/min until the tubes had been crushed axially a total of 50mm. Load and displacement of the crosshead were recorded. For the two tubes with the bevel trigger, the tube end with the bevel was placed upward.

Results from the experiment by Huang and Wang are reported as specific crushing stress (SCS) with units of N*m/g. The SCS of a specimen is defined by the crushing load (P), the specimen density (ρ), and the cross-sectional area of the tube (A) as follows

$$SCS = \frac{P}{\rho A} \tag{5.1.1}$$

Values for the SCS can be obtained for every data point using the instantaneous crushing load. By looking at the SCS at specific points, such as the initial peak, other parameters can be obtained to evaluate the crushing performance of the specimens. Using the mean

crushing load gives the mean SCS, also known as the specific energy absorption (SEA) of the specimen, also in N*m/g.

$$SCS_{mean} = SEA = \frac{E_{total}}{M_c} = \frac{\int_0^{L_c} Pds}{\rho A L_c} = \frac{\int_0^{L_c} SCSds}{L_c} \quad (5.1.2)$$

where E_{total}, M_c, and L_c are the total energy absorbed, the mass of the crushed material, and the length of the crushed region, respectively. SEA can then be used along with the peak SCS to obtain the crushing load efficiency (CLE).

$$CLE\ (\%) = \frac{P_{mean}}{P_{peak}} = \frac{{}^{P_{mean}}/_{\rho A}}{{}^{P_{peak}}/_{\rho A}} = \frac{SEA}{SCS_{peak}} \quad (5.1.3)$$

5.2 Thesis FE Model

The finite element model constructed in Abaqus is a dynamic non-linear explicit analysis. A 2-D sketch of a circle with a diameter equal to the mean diameter of the physical tube (51.83 mm) was extruded 100 mm to produce a cylinder geometrically identical to the physically tested specimen once the thickness is taken into account. This tube was placed between a rigid base plate which was constrained in all 6 degrees of freedom (DOF) and a rigid impactor plate free to move in the tube's axial direction (global y-axis) but constrained in the other 5 DOF. The physical geometry of the base plate holds the tube in place during the analysis so that the tube is not constrained numerically by any direct boundary conditions.

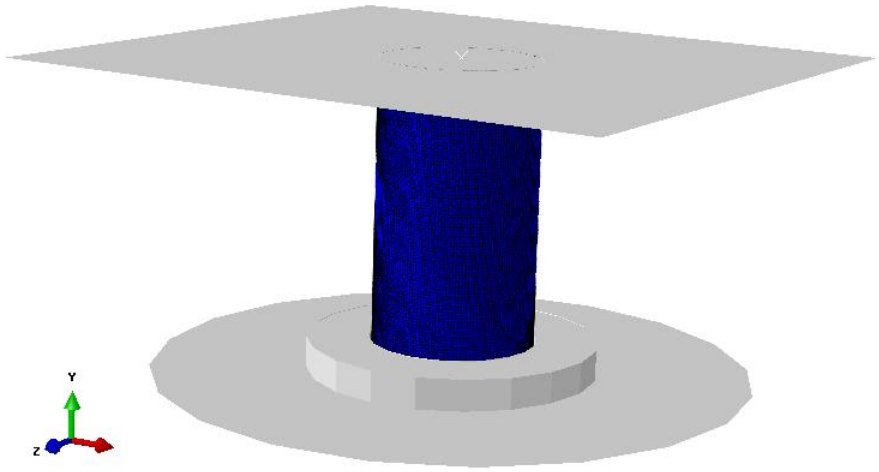

Figure 11. Thesis FE Model of Composite Tube.

The tube consists of 7,369 shell elements with a seed size of 1.5 mm. Elements in the first 5mm of the tube are 1.5mm x 1.5mm, while elements in the rest of the tube vary from 1.5mm x 2mm near the top to 1.5mm x 5mm at the base. A mesh convergence study was not performed due to the lack of completed runs, but the element size was assumed to be adequate based on the fact that multiple papers performing similar analyses [2, 6, 13] used elements that were equal or larger in size with accurate results.

Huang and Wang [2] discovered in their FE model that significant hourglassing occurred during the initiation of the crush zone when reduced integration elements were used. In order to prevent this, the first three rows of elements were fully integrated and the remaining elements were kept as reduced integration. The FE model constructed in this paper used this same approach, with the first 5 mm of the tube set to use fully integrated elements and the remainder using reduced integration elements with hourglass control. For all elements, the element deletion and stiffness degradation options were

toggled on. The value of d_{max} used was investigated and will be discussed in a later section.

Material properties for T700/QY8911 were entered along with damage initiation and evolution criteria. Two methods for modeling the composite layers were tested: one with a single shell representing all 14 plies and another with two stacked shells consisting of 7 plies each. The stacked shell model is capable of accounting for the delamination observed in the physical test whereas the single shell model is not. In order to accurately model the beveled edge, the tip of the tube in each model incorporates an additional material section with a reduced number of plies offset towards the inside diameter of the tube. This is another area where the stacked shell model can potentially perform better than the single shell model because the additional shell allows for a more gradual bevel. Figure 12 shows both models with the graphics set to show section thicknesses to illustrate the difference in the bevel.

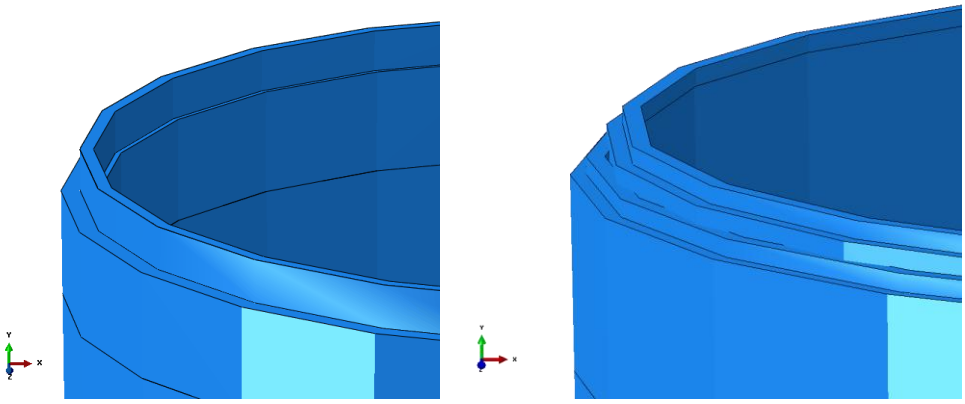

Figure 12. Single Shell (Left) and Two Shell (Right) Bevels.

Three contact interactions were specified: impactor to tube, base to tube, and the tube with itself. The contact interaction property for the first two contacts specified a

penalty formation and a tangential friction coefficient of 0.2 based on work performed by Zhu et al. [2, 26], which closely agrees with the 0.22 value used by McGregor et al. [12]. A tie constraint between the base surface and the bottom tube nodes was also used to ensure that the tube remained in contact with the base plate throughout the simulation. The impactor and base each contained a reference point in order to track displacement and reaction force, respectively. The impactor was given an initial velocity of 0.01 m/s in the -y (axial) direction, with an acceleration of $1 m/s^2$ in the same direction. The effects of changing the impact speed were also investigated because the experimental loading was quasi-static, although Obradovic et al. [9] and Basagni et al. [6] observed good correlation as high as 7.0 m/s and 8.4 m/s, respectively. The increase in velocity allowed the program to run more quickly since less time was needed for the tube to be crushed the same distance. The simulations were set to run for 0.31 seconds which allows for a total distance travelled by the impactor to reach 51 mm, 1mm more than the physical crush distance. Mass scaling was utilized in the form of scaling material density. Increasing the density by a factor of $1e^4$ decreased the run time from over 48 hours to approximately 4 hours. A computer with a 2.79 GHz dual-core 64 bit processor and 16 GB of RAM was used.

5.2.1. FE Model Target

Huang and Wang built an FE model of their own in order to simulate the results they obtained from crushing the composite tube [2]. Many of the analysis techniques used in this paper were adopted from their model. Figure 13 shows both their numerical results reported in terms of specific crushing stress (SCS) as well as the physical prediction from their model. These provide the target for the Abaqus model constructed in this paper.

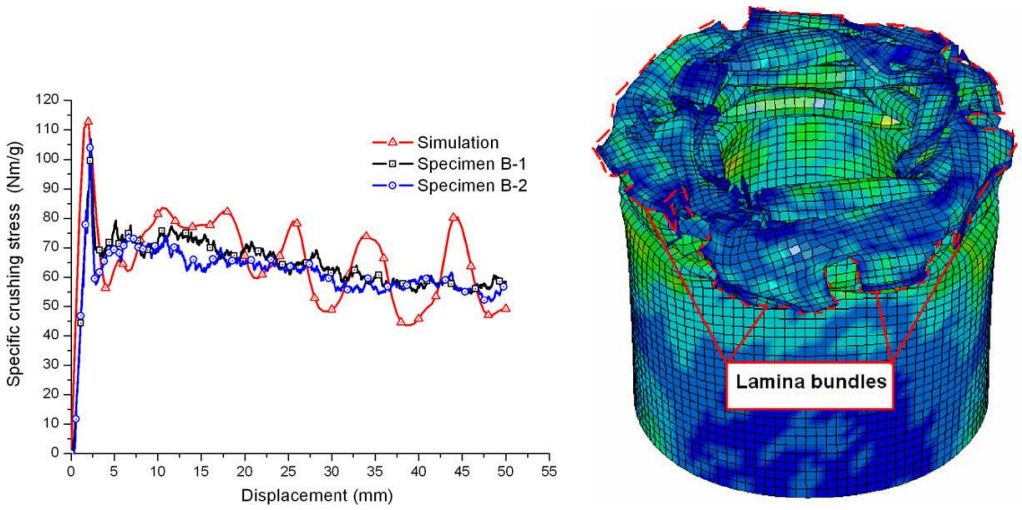

Figure 13. Numerical and Physical Predictions from Huang and Wang Simulation[2].

5.2.2. FE Model Development

Model development began with the single layer design, Hashin's 1980 damage initiation criteria, and the d_{max} variable set to 0.9. That run exited with an error after roughly 33% of its desired time: excessive distortion of an element. This error, or a closely related one (excessive rotation), would prove to be extremely difficult to overcome throughout the course of this project. However, this first run still continued long enough to simulate the crush initiation and evolution into a stable crush zone. Figure 14 shows the results at the end of the run and the lamina bundles described in the physical test can be seen starting to form. Some local buckling is starting to occur ahead of the crush zone below the bundles.

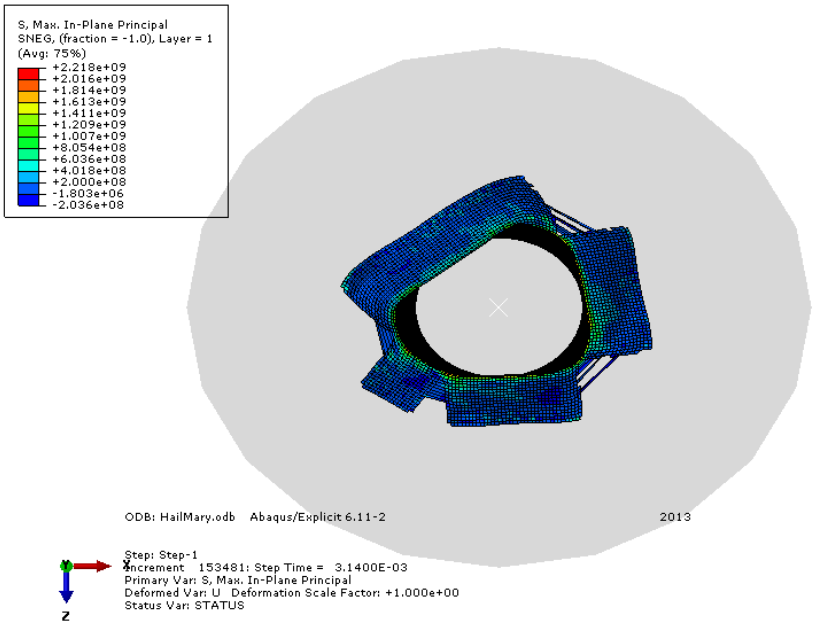

Figure 14. Top View of Single Layer Simulation Results Using Hashin's 1980 Criteria and d_{max}=0.9.

Switching to Hashin's 1973 criteria allowed the simulation to continue far past the point where the previous simulation stopped. It was stopped by the user after more than 66% completion without any errors because it had taken two days of computing time to reach that point. Figure 15 shows the progression of damage starting with the top and finishing with the bottom. The top image in Figure 15 was taken at the same moment in time as the images in Figure 14 to show their differences. Since the 1973 damage model does not include shear in the fiber tension failure mode or the middle term in the matrix compression failure mode, it is expected that failure is less likely to occur. The two images of the same point in time show a little bit of this occurring, with only 3 bundles forming when the 1973 model was used while 4 formed when the 1980 model was used. The extra bundle means that one extra failure area occurred as a result of the more damage-prone criteria of the 1980 model.

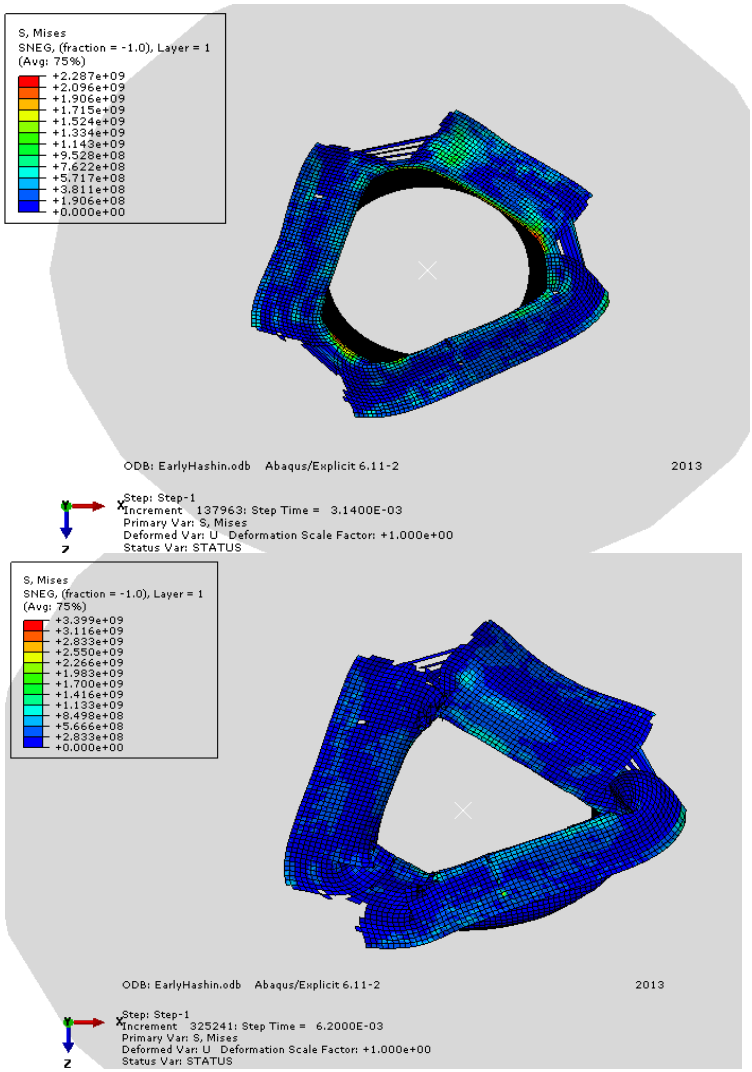

Figure 15. Top Views at Two Different Points in Time of Single Layer Simulation Results Using Hashin's 1973 Criteria and d_{max}=0.9.

The numerical results from the first two simulations are shown in Figure 16 below. Not surprisingly, all of the points before damage occurs are the same. Once damage has begun, even though the 1980 model appears to fluctuate more than the 1973 model they both experience peaks and valleys at the same time and follow each other extremely closely. A peculiar pattern is present in the data. The simulation using the 1980 model consistently has higher stress (force) peaks right before each time it drops off again. One possible explanation for this that agrees with the visual results is that since

damage initiation is less likely using the 1973 model, the material will buckle before it breaks. Since more energy is absorbed through fiber breakage than buckling, higher stresses are recorded.

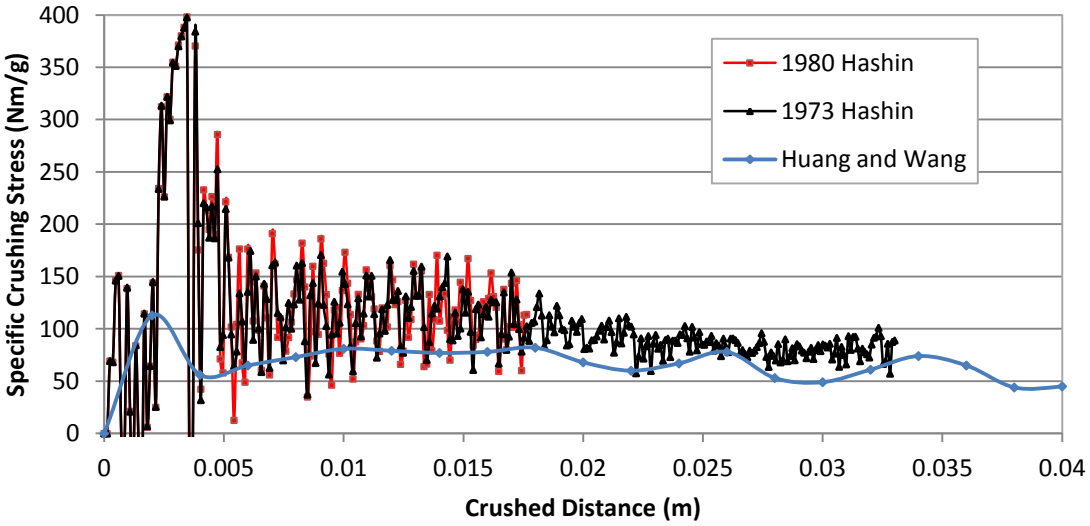

Figure 16. SCS of Hashin's Criteria with d_{max}=0.9.

Figure 16 shows that past about 22 mm of crushing, the values of SCS experience less dramatic fluctuation and are lower overall. The bottom image in Figure 15 shows how much buckling was occurring during this time period towards the end of the run. This again shows that local buckling absorbs less energy than fiber breakage.

Changing the maximum damage variable, d_{max}, is how damage evolution can be altered. Based on the results from the two runs, both damage models appear to give reasonable results but the value for d_{max} was set high enough that the tube displayed more plastic behavior than brittle failure.

The next test kept all variables the same but lowered d_{max} to 0.8. This caused the material to exhibit more brittle behavior with a greater number of individual fronds

breaking away. However, both of these runs exited with errors related to excessive element distortion. In a reversal of the first trials, the model using Hashin's 1980 criteria ran longer than the model using the 1973 criteria.

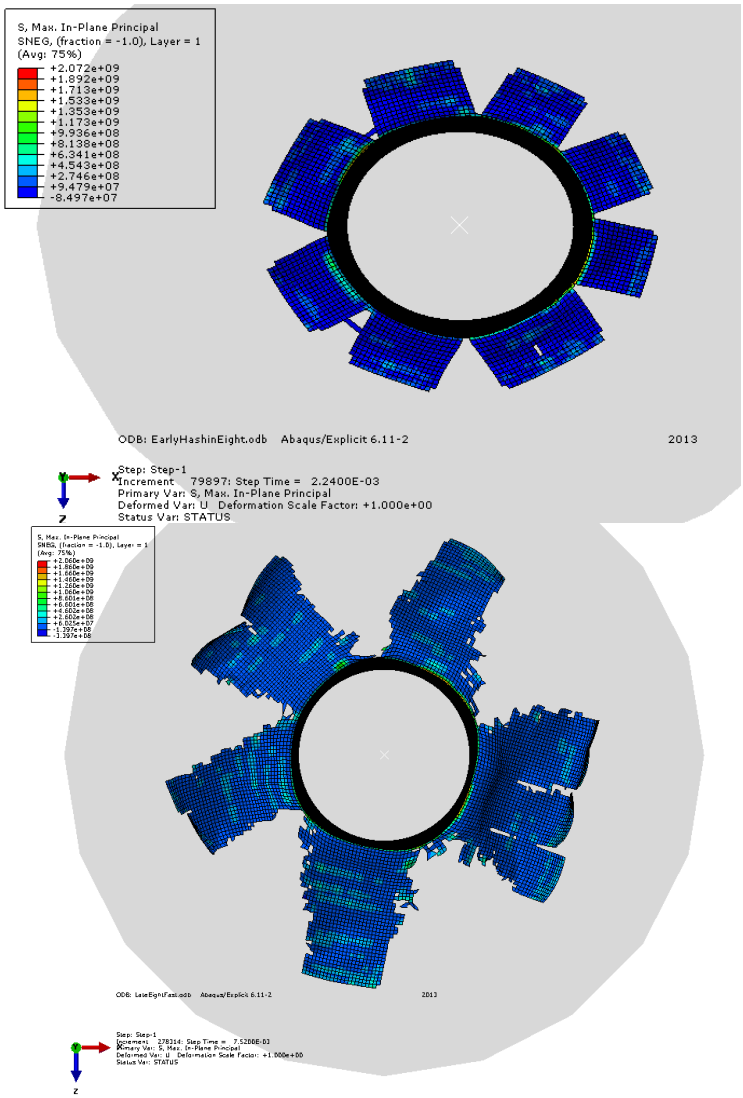

Figure 17. Top Views of Single Shell Simulation Results Using Hashin's 1973 (top) and 1980 (bottom) Criteria with d_{max}=0.8.

At this point, the mass had not been scaled in order to decrease computing time so other methods of potentially shortening run time were investigated. One such method involved reducing the number of integration points in each ply. Abaqus has the ability to construct a composite material section ply by ply, complete with fiber orientation and

number of integration points to be evaluated throughout the thickness of each ply. The default value is set at 3 points per ply, one at each edge and one in the middle. This number was reduced to one integration point per ply and the results are shown in Figure 18.

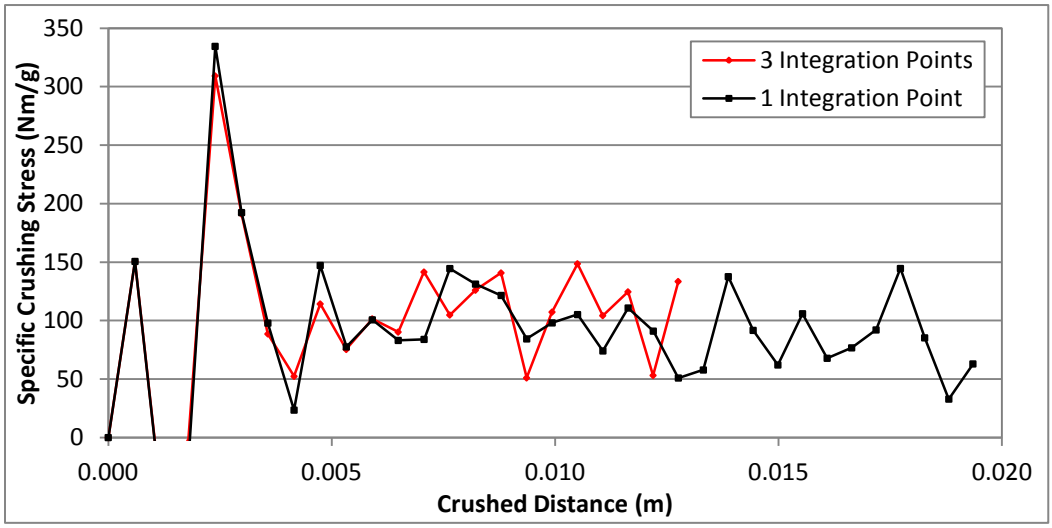

Figure 18. Comparing Effects of Number of Integration Points Used.

While the results do not match each other perfectly, the reduced number of integration points did not significantly change the results or behavior of the model. From this point on, only one integration point per ply was used for a total of 14 integration points throughout the material thickness.

After continued refinement, the decision was made to construct another model using two stacked shells in order to more accurately predict the physical response of the tube. It should be noted that no delamination effects were directly modeled; the shells were not bound together by any type of cohesive element that could model the energy absorbed through delamination. It was determined that this would still provide an accurate response based on the results displayed in Figure 5, showing that the amount of

energy absorbed through delamination is less than 3% of the total energy absorbed [12]. Figures 19 and 20 show the physical predictions and numerical results, respectively, of a refined stacked shell model.

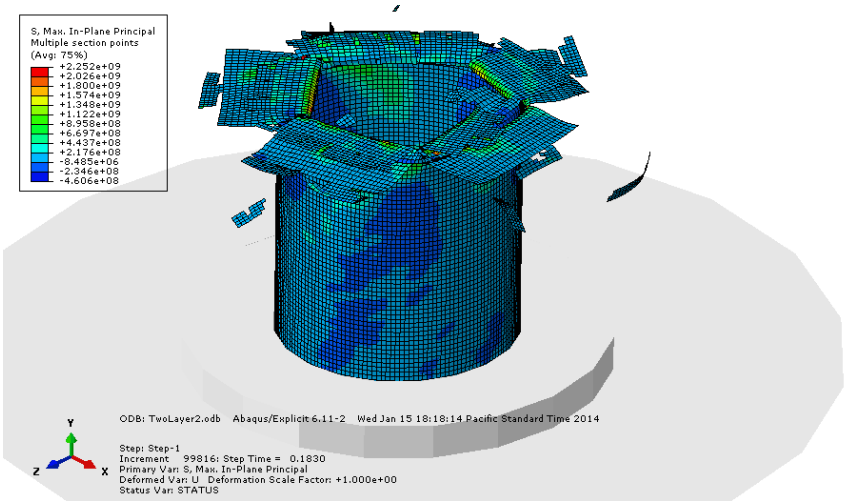

Figure 19. Isometric View of Stacked Shell Model.

This image shows that the stacked shell model much more closely replicates the behavior of the physical test than the single shell model did. Lamina bundles are forming both to the inside and outside of the tube whereas the single shell model only produced fronds to the outside. Looking at the numerical results in Figure 20, the stacked shell model has a much lower initial peak due to the more gradual bevel trigger and reduced d_{max} value for the top 5mm of the tube. Results from a single shell model with reduced d_{max} value for the same region are included for comparison.

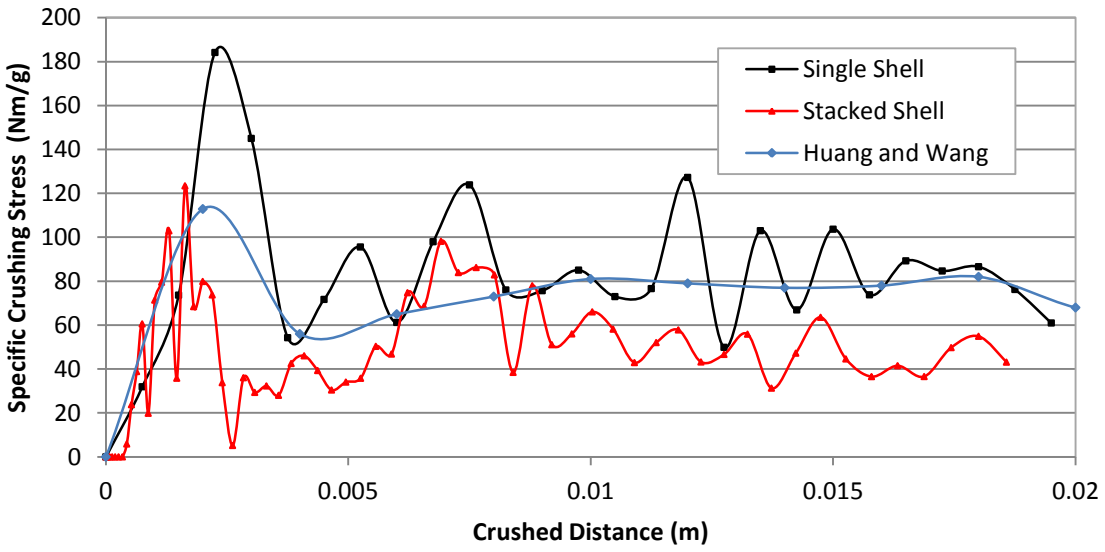

Figure 20. Numerical Results for Single and Stacked Shell Models.

Even after numerous improvements, the simulation would still exit with an error related to excessive element distortion. Looking at the results from the stacked shell model in Figure 20, some excessive oscillations can be seen during what is supposed to be the "stable" crush zone of the tube. Another test shortly after that one increased the density scaling from $1e^3$ to $1e^4$ and the problem became abundantly clear.

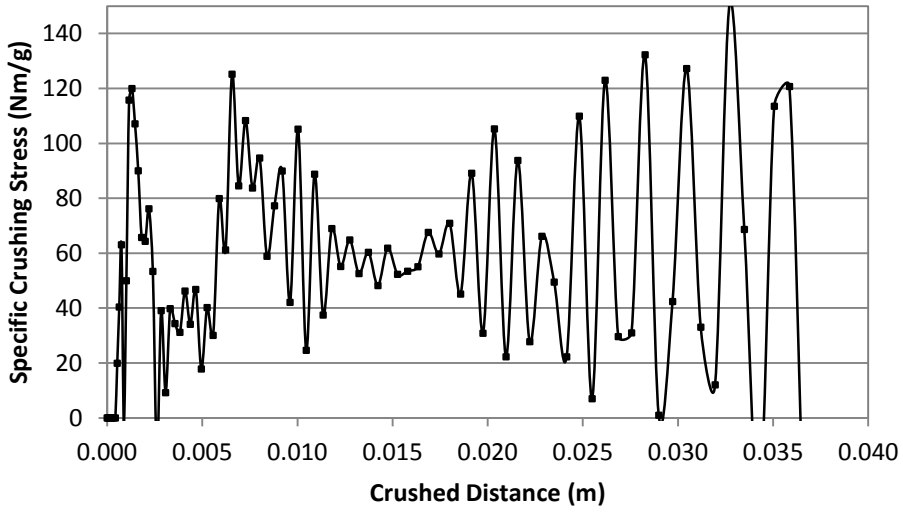

Figure 21. Stacked Shell Simulation with Damping Problems.

Some oscillation is to be expected based on results from Huang and Wang [2] but the amount displayed in Figure 21 is far too much. The simulation displayed characteristics of an under damped system with oscillations that became exponentially greater in amplitude. This pointed to an issue with the amount of damping within the model, which would also potentially explain the negative values observed toward the beginning of some of the runs.

There are a number of ways to introduce damping into an Abaqus model. Damping factors can be found under the contact interaction properties, bulk viscosity, and damage stabilization. Contact damping was the first type investigated. Increasing that factor from the default value of 0.03 to 0.08 resulted in a response that still oscillated but did not increase in amplitude like before. Further increasing the contact damping factor did not yield any significant improvement beyond this first adjustment.

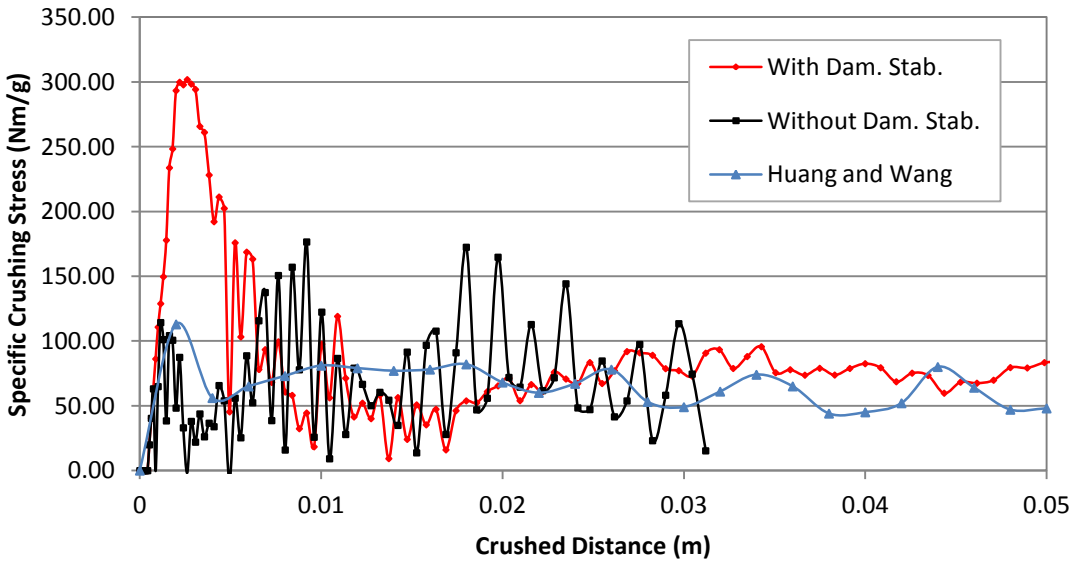

Figure 22. Stacked Shell Simulation with Increased Damping.

The introduction of damage stabilization coefficients in the four modes (longitudinal and transverse, compression and tension) greatly improved the numerical results of the simulation as shown in Figure 22. Even though the initial peak is almost three times as large as it should be, the stable crush zone that follows oscillates with much lower amplitude and predicts the correct range of specific crushing stress. However, Figure 23 shows how the physical predictions are not as accurate as the numerical results would suggest. No elements were damaged to the point of deletion and the tube displayed only plastic behavior without any lamina fronds or bundles forming.

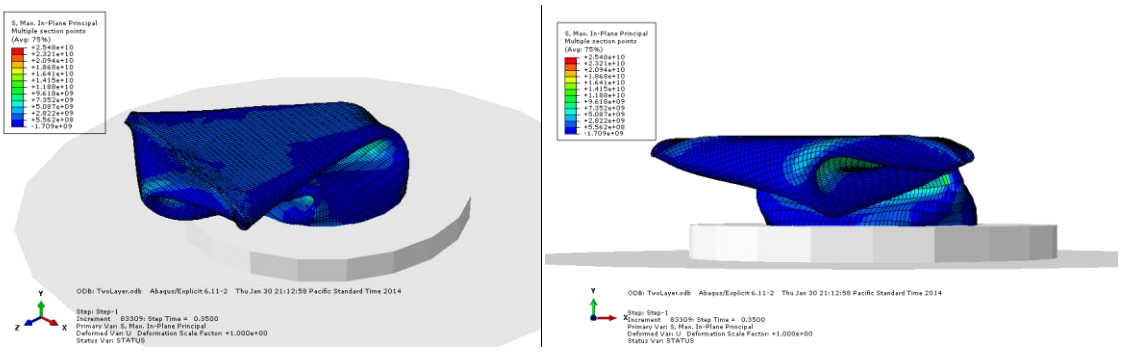

Figure 23. Isometric and Side Views of Model with Damage Stabilization.

The first trial with damage stabilization coefficients had them all arbitrarily set at 0.2 to serve as a starting point. Subsequent trials were performed with all values set equal to each other and also with only certain modes active. The tipping point is around $1e^{-5}$ regardless of which mode is set to that value. A value higher than that and the model will display the non-brittle behavior shown in Figure 23. A value lower than that will result in the model deforming properly but the run will once again abort with an error.

The final type of damping experimented with was the linear bulk viscosity parameter. There is also a quadratic bulk viscosity parameter available, but since it only affects solid continuum elements [23], not shell elements, it was ignored. The bulk viscosity parameter introduces an amount of numerical damping to the model; it is not a part of the material's constitutive response [23]. The default value within Abaqus is 0.06. Values ranging from 0.01 to 0.7 were tested with results pointing to a value of 0.5 being the most stable. If the value is set too high, the model would become unstable and shatter as shown in Figure 24.

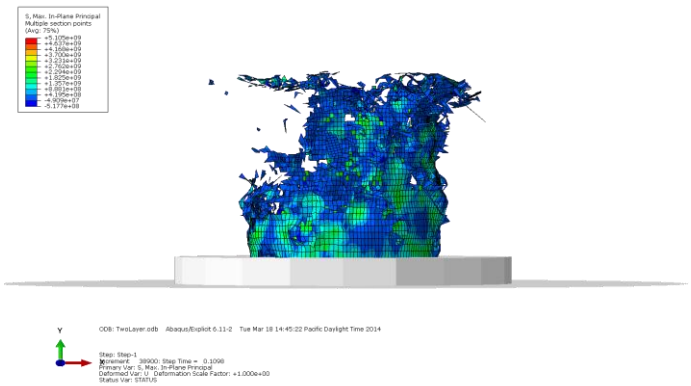

Figure 24. Model with Linear Bulk Viscosity Parameter Set Too High.

While increasing the contact damping fraction on its own did not yield any significant results, combining it with a larger linear bulk viscosity parameter had a positive effect on the outcome. Figure 25 shows the improved stability due to increasing the amount of damping present in the model. The simulation still exited with the usual error related to excessive element distortion but the results up until that point are much better.

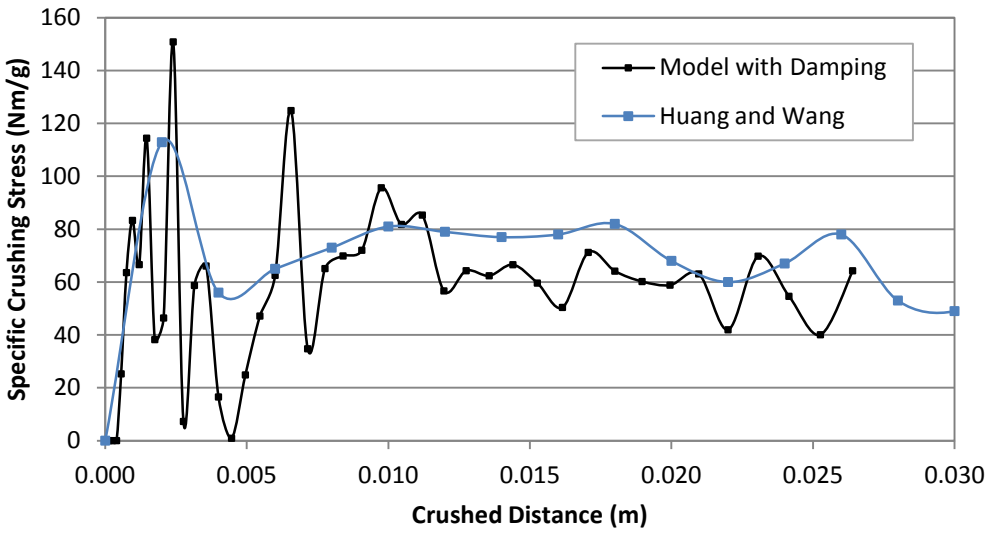

Figure 25. Stacked Shell Model with Contact and Bulk Viscosity Damping.

After the damping issue had been mostly sorted out, the same error was still present. The next approach to eliminating this error involved different methods for controlling hourglassing of reduced integration elements. Abaqus offers several options for hourglass control in an element. The default method is known as the integral viscoelastic approach which has more resistance to hourglassing at the beginning of the analysis than it does later on in the step [23]. This sounds like a good approach because the beginning of the step is when contact is initiated and the model experiences a step increase in loading. However, it is possible that this method would not provide enough resistance to hourglassing later in the step when most of the errors have been appearing. Switching to the pure stiffness method is recommended for quasi-static simulations and could help eliminate the error. Doing so allowed the simulation to continue much farther than before as shown in Figure 26.

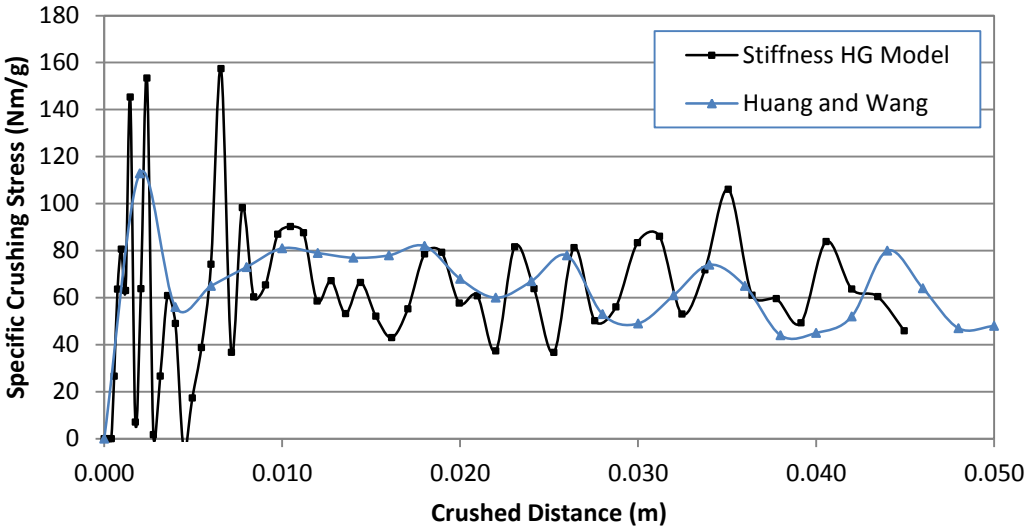

Figure 26. Model with Stiffness Hourglass Control.

Throughout the course of these different trials, the impact velocity was increased to 2m/s in order to allow for a shorter step time and speed up the simulation. Reducing the initial velocity to 0.01 m/s and imposing a $1m/s^2$ acceleration allows the initial contact to occur at a slower speed while not requiring the entire run to be performed at that low speed. This did not have much of an effect on the initial spike, but it did allow the model to proceed with less extreme oscillations.

Chapter 6. Results

6.1. Paper Experimental Results

Huang and Wang [2] observed that on specimens B-1 and B-2 the crush was initiated at the tube end with the 45° bevel as desired. Specimen B-0 did not have a bevel trigger so its crush began at the bottom of the tube. The inclusion of the beveled end greatly reduced the value of the initial peak load compared to the results from the non-beveled tube. After crushing had been initiated, all three specimens displayed very similar responses for how the crushing progressed. Figure 27 shows Huang and Wang's results plotted as specific crushing stress (SCS) vs. displacement.

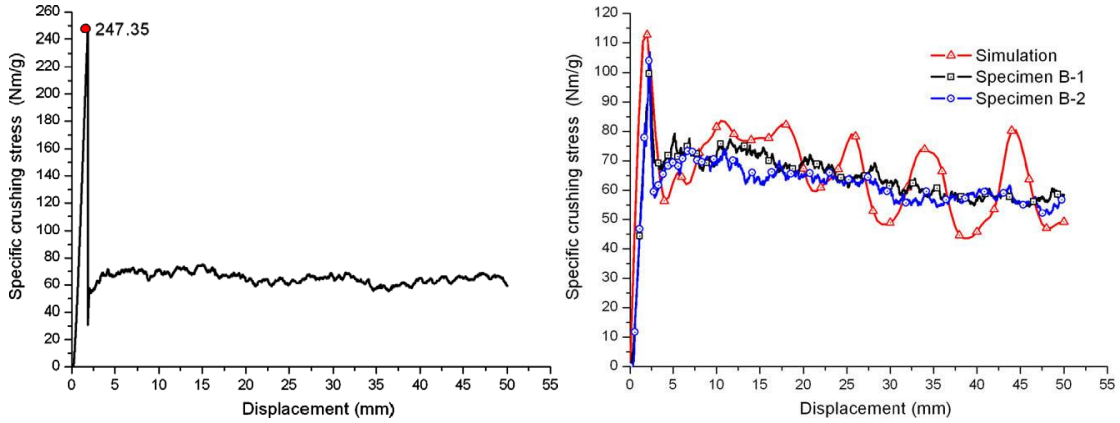

Figure 27. Stress-Displacement Curve of Specimen B-0 (left), B-1 and B-2 (right) [2].

Table 4. Experimental and Numerical Results [2].

Specimen	SCS_{peak} (Nm/g)	SEA (J/g)	CLE (%)
B-0 (without trigger)	247.35	66.48	26.88
B-1 (with bevel trigger)	101.44	64.05	63.14
B-2 (with bevel trigger)	106.85	61.40	57.46
Average of B-1 and B-2	104.15	62.73	60.23
Huang and Wang FE Results	112.88	66.11	58.57

Running the experiments, Huang and Wang noted that "stable progressive crushing processes with a brittle fracturing crushing mode, shown in [Figure 28], were

observed for all specimens" [2]. The tube wall delaminated into three distinct layers: interior layer, middle layer, and exterior layer as they are referred to by Huang and Wang. The interior layer bent inward toward the center of the tube while the middle layer formed "lamina bundles" which bent outward. Huang and Wang concluded that delamination of the tube wall and bending/fracture of these lamina bundles were the primary contributors to the energy absorption of the tube [2].

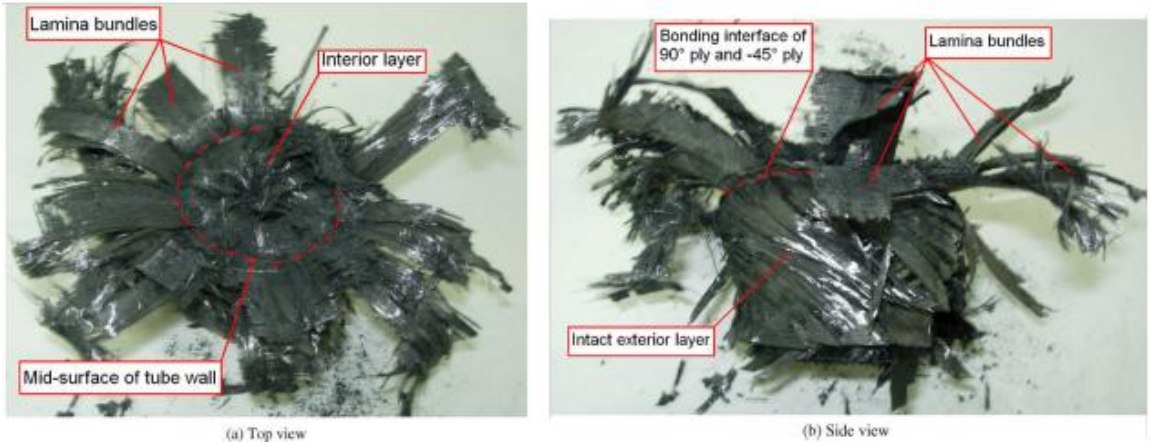

Figure 28. Physical Experimental Results [2].

6.2. Thesis FE Results

After many failed trials, the final model came reasonably close to predicting the response observed by Huang and Wang. The numerical response shown in Figure 29 displays an initial spike followed by the development of a stable crush zone as expected.

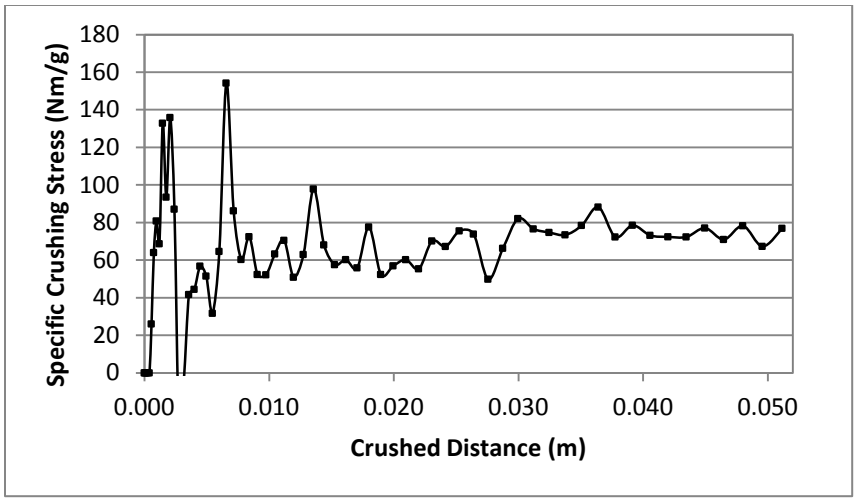

Figure 29. Thesis Numerical Results.

Likewise, the model's prediction for the physical response of the tube is in agreement with what is expected. Multiple fronds form which deflect either inwards or outwards depending on which shell of the tube they are. There is local buckling occurring ahead of these fronds to form bundles similar to what is described in the paper.

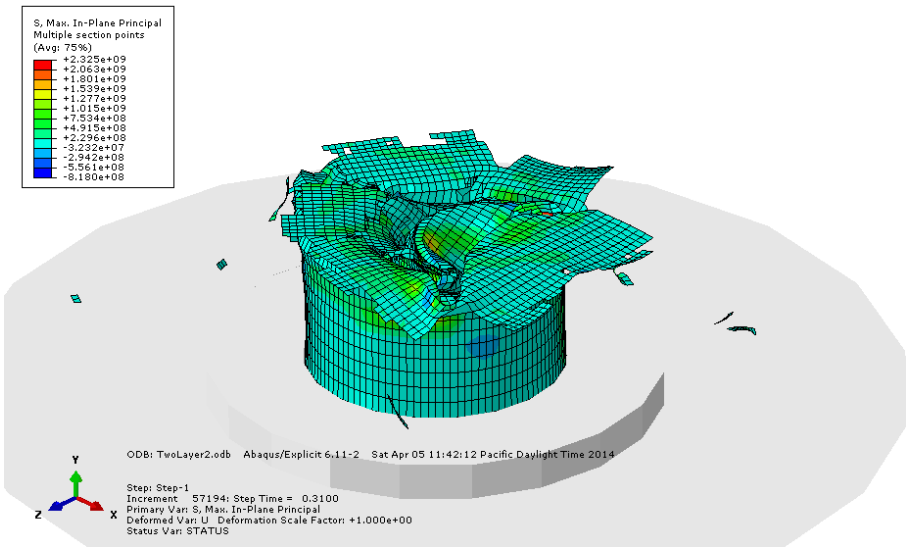

Figure 30. Thesis Physical Predictions.

The thesis model also agrees for the most part with the results from Huang and Wang's model, as shown in Figures 31 and 32. A couple of discrepancies are present,

however. The first is that the initial spike predicted by Abaqus is 20% higher than the one predicted by Huang and Wang [2], although they do occur at the same time. After the initial spike, the thesis model shows a short period of extreme oscillation, highlighted by two points with negative values and a second spike consisting of a single point. This could possibly be explained by some sort of damping issue remaining within the model. The last difference is, past 30mm of crushing, the thesis model predicts higher stresses than the physical test showed. Whereas the results from Huang and Wang show a slight decrease in SCS as the crush progresses, the thesis model shows an opposite trend. Huang and Wang included a softening factor in their analysis model to account for crack propagation ahead of the crush zone [2] which is the most likely the reason for the downward slope.

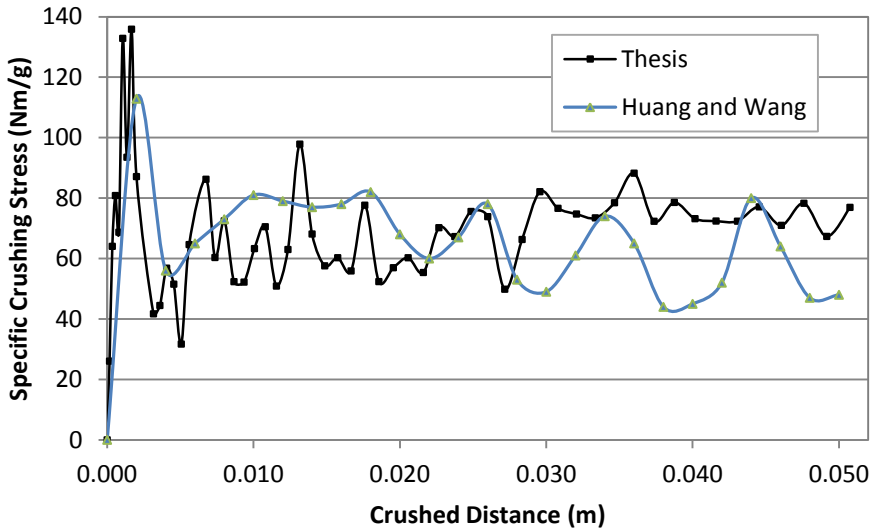

Figure 31. Thesis and Huang and Wang [2] Numerical Results.

The image used by Huang and Wang to illustrate the physical response as predicted by the FE model appears to be from a moment somewhere in the middle of the run, not at the end. The approximate time was estimated based on physical appearance

and an image from the thesis model at the appropriate time is shown below for more direct comparison.

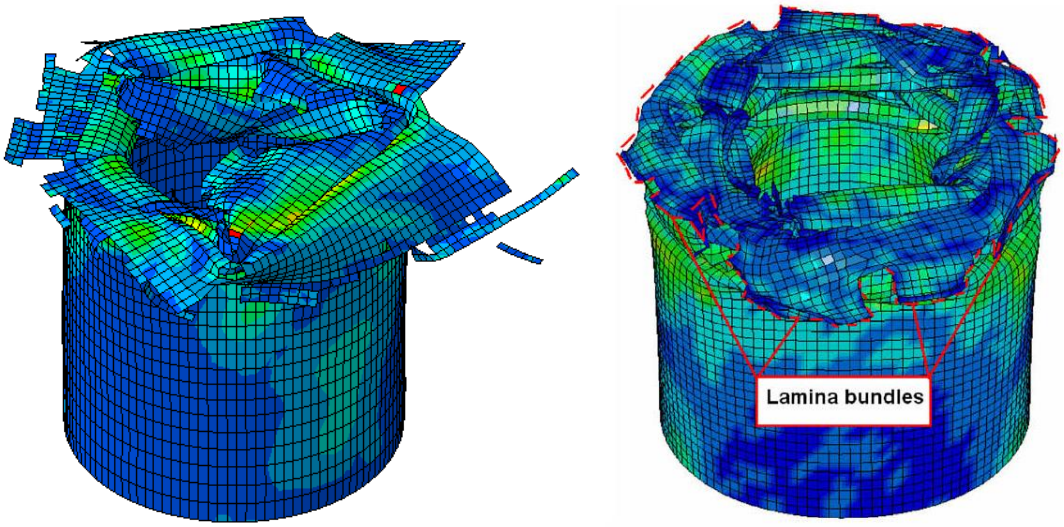

Figure 32. Thesis (left) and Huang and Wang [2] (right) Physical Predictions.

Both models are show similar trends at this point in the simulation. The two layers of the tube can be seen displaced both inward and outward with local buckling occurring ahead of the contact zone to form bundles. Complete material failure has occurred in multiple areas as evidenced by the number of elements that have been deleted from the simulation.

6.3. Discussion

Unfortunately, the run being discussed is the only complete run which also predicted the correct physical response of the tube. A handful of other simulations were completed with promising numerical results but their physical responses were wildly inaccurate. Although model stability was a recurring problem which was never fully solved, other runs still yielded some very accurate results. Table 5 compares the peak specific crushing stress, specific energy absorbed, and crush load efficiency of the model

discussed in the previous section, an incomplete model, and results from Huang and Wang.

Table 5. Comparison of Thesis and Huang and Wang [2] Results.

Specimen	SCS_{peak} (Nm/g)	SEA (J/g)	CLE (%)
Thesis Model 1 (completed, 50mm)	135.90	68.03	50.06
Thesis Model 2 (aborted, 36mm)	102.39	61.41	59.65
Average of B-1 and B-2	104.15	62.73	60.23
Huang and Wang FE Results	112.88	66.11	58.57

The results from this incomplete model, as well as those from many other incomplete simulations, lead to the conclusion that even though stability is an issue, accuracy is not. Many different approaches were taken to improve stability. The only time the model consistently completed simulations was when damage stabilization was used and no elements were deleted. Even though the physical results were inaccurate, the numerical results were accurate after the initial spike.

Excessive hourglassing could have potentially caused the repeated error, but the same error still caused the simulation to abort during a run using only fully integrated elements. Another possible cause of the error is that the linear damage evolution technique shown in Figure 24 was set with the post-damage slope too steep. Since the composite modeled has a brittle fracture behavior, the response drops off sharply once the failure limit has been reached. If the computer predicted even a slight increase in strain at that point, the extremely sensitive response could cause instability within the model. To test this theory, the value for fracture energy of each mode was increased by 10% to lessen the severity of the drop and the simulation run again. No significant improvements were observed.

Not including the effects of delamination did not have a significant effect on the results. Both the physical and numerical results match very closely with the target, suggesting that modeling delamination may be unnecessary. Accurately modeling initial contact response and crush initiation was challenging. Values for maximum degradation were reduced in the trigger area in an attempt to reduce the initial spike, although reducing the maximum degradation value of the rest of the tube had an effect as well.

Chapter 7. Conclusion

The largest issue involved with modeling this system is stability. The root cause of the excessive element distortion/rotation errors was never uncovered. Further investigation needs to be carried out in eliminating this error if the model is to become stable. Several important parameters were determined throughout the course of this project:

- The FE model was able to accurately predict the forces involved and energy absorbed. However, even though physical deformation predicted by the model closely matched that from the paper, it struggled with predicting the actual failure modes exhibited by the physical tube.
- Mass scaling had a substantial effect on computer run time because it allowed the stable time increment to increase. It did not have any noticeable effects on the accuracy of the results.
- Using only one integration point per ply reduced the run time without reducing the accuracy.
- Material damping through linear bulk viscosity, as well as contact damping, helped stabilize the system by reducing vibrations inherent with the analysis.
- Damage stabilization did not allow for any complete element failure to occur.
- Stiffness hourglass control provided better resistance to hourglass modes later in the run, which reduced spikes in what should have been the stable crush zone.
- Hashin's 1980 failure criteria gave a smoother response than the 1973 criteria due to the contribution of multiple stresses to certain failure modes.

- Adding 10% to the fracture energy to make the response more gradual from the strain point at damage initiation to the strain point at failure did not help with stability.
- Maximum degradation factor of 0.85 allowed the simulation to complete the one run. A factor of 0.80 gave much more accurate results even though it did not complete.
- The model still produced accurate results even without including delamination energy. Using two layers of plies to simulate the effects of delamination without any cohesive elements was adequate.
- Modeling first contact and crush initiation requires great care. Slower velocities during this time help.
- A mesh size of 1.5mm x 1.5mm for the trigger, blending into 1.5mm x 5mm at the base, provided a good balance between accuracy and time requirements.

Even though simulation stability was a major issue, the model proved to be accurate both in regards to the SCS-displacement curves and physical failure mode. Lessons learned from developing this model can be used to construct another model and accurately predict the crushing response of the 3D FSAE nose cone.

REFERENCES

[1] SAE International, "2013 Formula SAE Rules," 2012.

[2] Huang, J. and Wang, X., "Numerical and Experimental Investigations on the Axial Crushing Response of Composite Tubes," Composite Structures, vol. 91, issue 2, pp.222-228, 2009.

[3] Savage, G., Bomphray, I., and Oxley, M., "Exploiting the Fracture Properties of Carbon Fibre Composites to Design Lightweight Energy Absorbing Structures," Anales de Mecánica de la Fractura, vol. 20, 2003.

[4] Savage, G., "Formula 1 Composites Engineering," Engineering Failure Analysis, vol. 17, 2010.

[5] Savage, G., "Development of Penetration Resistance in the Survival Cell of a Formula 1 Racing Car," Engineering Failure Analysis, 2010.

[6] Bisagni, C., Di Pietro, G., Frashini, L., and Terletti, D., "Progressive Crushing of Fiber-Reinforced Composite Structural Components of a Formula One Racing Car," Composite Structures, vol. 68, pp.491-503, 2005.

[7] Belingardi, G. and Obradovic, J., "Design of the Impact Attenuator for a Formula Student racing Car: Numerical Simulation of the Impact Crash Test," Journal of the Serbian Society for Computational Mechanics, vol. 4, issue 1, pp. 52-65, 2010.

[8] Boria, S. and Forasassi, G., "Progressive Crushing of a Fiber Reinforced Composite Crash-Box for a Racing Car," DIMNP, University of Pisa, 2009.

[9] Obradovic, J., Boria, S., and Belingardi, G., "Lightweight Design and Crash Analysis of Composite Frontal Impact Energy Absorbing Structures," Composite Structures, vol. 94, pp. 423-430, 2012.

[10] Belingardi, G. and Obradovic, J., "Crash Analysis of Composite Sacrificial Structure for Racing Car," Politecnico di Torino Department of Mechanics, vol. 37, No. 2, 2011.

[11] Abdel-Haq, M. and Newaz, G. M., "Role of Failure Modes on Energy Absorption in Unidirectional PMC Tubes," Journal of Composite Materials, vol. 35, No. 11, 2001.

[12] McGregor, C., Vaziri, R., and Xiao, X., "Finite Element Modeling of the Progressive Crushing of Braided Composite Tubes Under Axial Impact," International Journal of Impact Engineering, vol. 37, pp. 662-672, 2010.

[13] Xiao, X., "Modeling Energy Absorption with a Damage Mechanics Based Composite Material Model," Journal of Composite Materials, vol. 43, No. 5, 2009.

[14] Agarwal, Bhagwan D., Lawrence J. Broutman, and K. Chandrashekhara. Analysis and performance of fiber composites. Hoboken, NJ: John Wiley, 2006.

[15] Mello, Joseph D., "ME412: Design and Analysis of Composite Materials." California Polytechnic State University, San Luis Obispo. Class notes. San Luis Obispo, CA, 2013.

[16] Jones, Robert M. Mechanics of Composite Materials. Philadelphia, PA: Taylor & Francis, 1999.

[17] Tsai, S.W. and Pagano, N.J., "Invariant Properties of Composite Materials," Composite Materials Workshop, St. Louis, July 13-21, 1967, Technomic, Westport, CT, 1968.

[18] Goh, S., Ku, H., and Ang, S.L., "Prediction of Crushing Stress in Composite Materials," Journal of Composite Materials, vol. 42, No. 5, 2008.

[19] "Abaqus Theory Manual (v6.8)." Abaqus Theory Manual (v6.8). 2013 <http://mse-license1.mse.drexel.edu/v6.8/books/stm/default.htm>.

[20] Cook, Robert Davis. Concepts and applications of finite element analysis. New York, NY: Wiley, 2001.

[21] Hashin, Z., and A. Rotem, "A Fatigue Criterion for Fiber-Reinforced Materials," Journal of Composite Materials, vol. 7, pp. 448–464, 1973.

[22] Hashin, Z., "Failure Criteria for Unidirectional Fiber Composites," Journal of Applied Mechanics, vol. 47, pp. 329–334, 1980.

[23] "Abaqus Analysis User's Manual (v6.8)." Abaqus Analysis User's Manual (v6.8). 2013 <http://mse-license1.mse.drexel.edu/v6.8/books/usb/default.htm>.

[24] Matzenmiller, A., Lubliner, J., and Taylor, R.L., "A Constitutive Model for Anisotropic Damage in Fiber-Composites," Mechanics of Materials, vol. 20, pp. 125-152, 1995.

[25] "Abaqus/CAE User's Manual (v6.8)." Abaqus/CAE User's Manual (v6.8). 2013 <http://mse-license1.mse.drexel.edu/v6.8/books/usi/default.htm>.

[26] Zhu, B., Wang, C., and Cai, X., "Research of Influence Factors on Friction Coefficient of Carbon Fiber Reinforced Composite," Journal of Material Science Engineering, vol. 20, No. 3, pp. 361-363, 2002.

APPENDIX A

Calculation of total energy dissipated during damage, G^c.

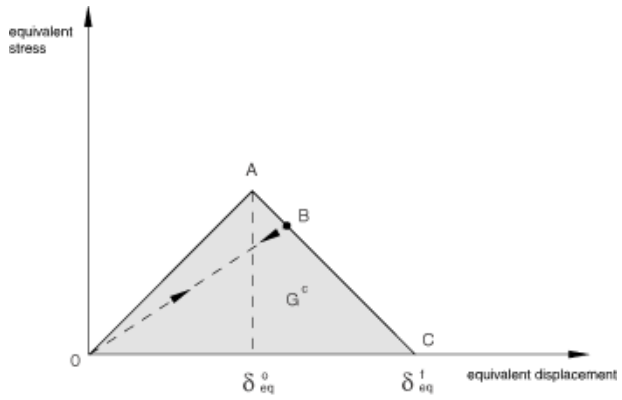

Figure 10 (Reproduced). Linear Damage Evolution [23].

Using the Young's Modulus, E_F, and compressive strength, S_{FC} to calculate the failure strain, ε_{FC}^u, for the fiber compressive direction,

$$S_{FC} = E_F * \varepsilon_{FC}^u$$

Rearranging,

$$\varepsilon_{FC}^u = \frac{S_{FC}}{E_F}$$

Then using S_{FC} and ε_{FC}^u to calculate the total energy dissipated,

$$G_{FC}^C = \frac{1}{2} * S_{FC} * \varepsilon_{FC}^u$$

The characteristic length, L_C, used in calculating the equivalent displacement shown in Figure 10 is taken into account by Abaqus so it does not need to be used in this equation here. G^C, as it is shown here, is the value which must be input into Abaqus' damage evolution model. This equation gives a vertical line from point A to point C.

APPENDIX B

Single shell models.

Run	Notes	Results
1	Hashin 1980, dmax=0.9, V=-1m/s initial	Aborted, 31% complete, 23h
2	Hashin 1973	User stopped, 62%, 48h
3	1980, dmax=0.8	User stopped, 75%, 24h
4	1973	Aborted, 22%, 10h
5	1 int. pt.	Aborted, 35%, 7h
6	1980	User stopped, 35%, 25h
7	1973, dtrig=0.65, dtube=0.75	Aborted, 47%, 10h
8	Same as (1), V constant	Aborted, 66%, 3.6h
9	V=-0.1 constant	User stopped, 1.7%, 23h
10	1973, dtrig=0.7, dtube=0.75, V=-1 constant	User stopped, 18%, 30h
11	1.7x1.7 elements	Aborted, 53%, 4h
12	dmax=0.9	Aborted, 26%, 15h
13	2.2x2.2	Completed, 100%, 1.5h
14	Same as (5), 2.0x2.0	Aborted, 46%, 2.5h
15	1980	Aborted, 27%, 1h
16	1.7x1.7 elements	Aborted, 40%, 4h
17	density x 10000, contact damping=0.1, Vo=-0.01m/s, A=-2m/s2, dtrig=0.65, dtube=0.8, enhanced HG control	Aborted, excessive distortion (1 elem)

Stacked Shell Models

Run	Notes	Results
1	1980, dtrig=0.75, dtube=0.8, 1 int. pt. 1.7x1.7, -4m/s const.	Aborted, excessive distortion
2	dtrig=0.65, 1x1 trigger to 1x3 tube elements, -2m/s const.	Aborted, excessive distortion
3	-1m/s const.	Aborted, wave speed
4	1x1 to 1x3 gradual transition elements	Aborted, wave speed
5	mass scaled x1000, fail strain added	Aborted, excessive distortion/rotation. Much faster
6	enhanced HG control	Aborted, excessive distortion
7	dtube=0.75 1x1.5 to 1x2 gradual transition elements	Aborted, excessive rotation
8	1x1.5 constant mesh, fail strain removed	Aborted, excessive distortion
9	dtube=0.8, V=-0.5 m/s const. 2mm more of FI elements (5mm total)	Aborted, excessive distortion
10	Vo=-0.01 m/s, A=-1m/s, 1x1.4 elements	Aborted, excessive distortion
11	A=-2m/s2, 1x1 to 1x1.4 gradual transition elements	Aborted, excessive distortion
12	A=-1m/s2	Aborted, excessive distortion
13	density x 10000	Aborted, excessive distortion
14	1x1 to 1x4 elements, contact damping =0.08	Aborted, excessive distortion
15	contact damping=0.2	Aborted, excessive distortion
16	Damage stabilization all =0.2	Completed, no elements deleted
17	Damage stabilization all =0.1	Completed, no elements deleted
18	Damage stabilization all =0.01	Completed, no elements deleted
19	Damage stabilization all =0.001	Completed, no elements deleted
20	Damage stabilization all =0.005	Completed, no elements deleted
21	dtrig=0.3, dtube=0.4	Completed, no elements deleted
22	dmax=0.1	Completed, no elements deleted
23	Damage stabilization all=5e-5	Completed, no elements deleted
24	Damage stabilization all=5e-7	Aborted, excessive distortion
25	Damage stabilization all=5e-6	Aborted, excessive distortion
26	Damage stabilization FC=5e-5	Aborted, excessive distortion
27	Damage stabilization FT=5e-5	Aborted, excessive distortion

28	Damage stabilization MC=5e-5	Aborted, excessive distortion
29	Damage stabilization MT=5e-5	Aborted, excessive distortion
30	No damage stabilization, contact damping =0.15, linear bulk viscosity=0.15, dtrig=0.65, dtube=0.87, 1x1 to 1x4 elements, stiffness HG control (Disp HG scaling factor=0.5, Rot HG=0.5)	Aborted, excessive rotation
31	Disp HG=2, Rot HG=2, Linear bulk viscosity=0.3	Aborted, excessive distortion
32	Disp HG=0.2, Rot HG=0.2, contact damping =0.25	Aborted, excessive rotation
33	1x1 to 1x3 elements	Aborted, excessive rotation
34	1x1 to 1x2 elements	Aborted, excessive rotation
35	Rot HG=0.1	Aborted, excessive rotation
36	dtrig inner=0.5, dtrig outer=0.65, Rot HG=1	Aborted, excessive distortion
37	Linear bulk viscosity=0.5, contact damping 0.35	Aborted, excessive rotation
38	Vo=-0.1m/s	Aborted, excessive rotation
39	V=-.2m/s const. Linear bulk viscosity=0.7	Aborted, excessive rotation
40	Contact damping=0.75	Aborted, excessive rotation
41	Contact damping=0.25, Linear bulk viscosity=0.5	Aborted, excessive rotation
42	Contact damping=0.5	Aborted, excessive distortion
43	Everything fully integrated	Aborted, excessive distortion
44	Back to Red. Int. for tubes, 1.5x1.5 for trigger, 1.5x2 to 1.5x5 for rest	Aborted, excessive distortion
45	Disp HG=1, Rot HG=1, Vo=-0.01m/s, A=-1m/s2	Completed
46	1x1 trigger, 1x1 to 1x3 tube, Disp HG=0.2, Rot HG=0.1	Aborted, excessive distortion
47	Same as (45), 1.5x1.5 to 1.5x4 tube, damage stabilization all=5e-6	Aborted, excessive distortion
48	Same as (45), damage stabilization all=5e-6	Aborted, excessive distortion
49	Same as (45), 1.5x1 trigger, 1.5x1.5 to 1.5x4 tube	Aborted, excessive distortion
50	Same as (45), dmax=0.8	Aborted, excessive distortion
51	Same as (50), fracture energy +5%	Aborted, excessive distortion
52	Same as (50), fracture energy +10%, Disp HG=0.2, Rot HG=0.1	Aborted, excessive distortion
53	Same as (52), Disp and Rot HG=1	Aborted, excessive distortion
54	Same as (52), Disp and Rot HG=1.4	Aborted, excessive distortion
55	Same as (52), Disp and Rot HG=1.8	Aborted, excessive distortion

APPENDIX C

Abaqus input file (condensed by removing individual element and node coordinates).

```
*Heading
** Job name: TwoLayer Model name: TwoLayer
** Generated by: Abaqus/CAE 6.11-2
*Preprint, echo=NO, model=NO, history=NO, contact=NO
**
** PARTS
**
*Part, name=Base
*End Part
**
*Part, name=Impactor
*End Part
**
*Part, name=OuterTube
*Node
      1, -0.0263724998,           0., 0.0939999968
      2, -0.0263724998,           0., 0.0984999985
      3, -0.0258603636, 0.00517207291, 0.0984999985

   4927, -0.00150137511, -0.0263297297, 0.00782008562
   4928, -0.0015023892, -0.026329672, 0.00396279711

*Element, type=S4
  1,   1,  19, 537,  55
  2,  19,  20, 538, 537

4815, 216, 535, 536, 217
4816, 217, 536,   9,   8

*Element, type=S4R
 337,   15,  249,  753,  402
 338,  249,  250,  754,  753

4787, 4927, 4928,  347,  346
4788, 4928,  509,   16,  347

*Nset, nset=_PickedSet6, internal
    1,    2,    3,    4,    5,    6,    8,   11,   13,   14,
15,   16,   18,   19,   20,   21

 4913, 4914, 4915, 4916, 4917, 4918, 4919, 4920, 4921, 4922,
4923, 4924, 4925, 4926, 4927, 4928

*Elset, elset=_PickedSet6, internal
    1,    2,    3,    4,    5,    6,    7,    8,    9,   10,
11,   12,   13,   14,   15,   16
```

```
 4773, 4774, 4775, 4776, 4777, 4778, 4779, 4780, 4781, 4782,
4783, 4784, 4785, 4786, 4787, 4788

*Nset, nset=_PickedSet7, internal
   2,   3,   4,   7,   8,   9,  10,  11,  12,  17,  23,  24,  25,
26,  27,  28

521, 522, 523, 524, 525, 526, 527, 528, 529, 530, 531, 532, 533,
534, 535, 536

*Elset, elset=_PickedSet7, internal
  141,  142,  143,  144,  145,  146,  147,  148,  149,  150,
151,  152,  153,  154,  155,  156

 4801, 4802, 4803, 4804, 4805, 4806, 4807, 4808, 4809, 4810,
4811, 4812, 4813, 4814, 4815, 4816

*Nset, nset=_PickedSet8, internal, generate
    1,  4928,     1

*Elset, elset=_PickedSet8, internal, generate
    1,  4816,     1

** Region: (SevenTube:Picked), (Controls:EC-3), (Material
Orientation:Picked)
*Elset, elset=_I1, internal
    1,    2,    3,    4,    5,    6,    7,    8,    9,   10,
11,   12,   13,   14,   15,   16

 2701, 2702, 2703, 2704, 2705, 2706, 2707, 2708, 2709, 2710,
2711, 2712, 2713, 2714, 2715, 2716

** Section: SevenTube
*Shell Section, elset=_I1, composite, controls=EC-3, layup="All
Layers"
0.0001307, 1, T700/QY8911, 45.
0.0001307, 1, T700/QY8911, -45.
0.0001307, 1, T700/QY8911, 90.
0.0001307, 1, T700/QY8911, 0.
0.0001307, 1, T700/QY8911, 0.
0.0001307, 1, T700/QY8911, 90.
0.0001307, 1, T700/QY8911, 0.
** Section: Trigger
*Shell Section, elset=_PickedSet7, composite, controls=EC-3,
offset=SPOS, layup=Trigger
0.0001307, 1, T700/QY8911, 45.
0.0001307, 1, T700/QY8911, -45.
0.0001307, 1, T700/QY8911, 0.
0.0001307, 1, T700/QY8911, 90.
** Region: (SevenTube:Picked), (Controls:EC-2), (Material
Orientation:Picked)
```

```
*Elset, elset=_I3, internal
  337,  338,  339,  340,  341,  342,  343,  344,  345,  346,
347,  348,  349,  350,  351,  352

 4773, 4774, 4775, 4776, 4777, 4778, 4779, 4780, 4781, 4782,
4783, 4784, 4785, 4786, 4787, 4788

** Section: SevenTube
*Shell Section, elset=_I3, composite, controls=EC-2, layup="All
Layers"
0.0001307, 1, T700/QY8911, 45.
0.0001307, 1, T700/QY8911, -45.
0.0001307, 1, T700/QY8911, 90.
0.0001307, 1, T700/QY8911, 0.
0.0001307, 1, T700/QY8911, 0.
0.0001307, 1, T700/QY8911, 90.
0.0001307, 1, T700/QY8911, 0.
*End Part
**
*Part, name=Tube
*Node
      1, -0.0254574995,           0., 0.0939999968
      2, -0.0254574995,           0., 0.0995000005

   4859, -0.00150813628, -0.0254127886, 0.00782008562
   4860, -0.00150938553, -0.0254127141, 0.00396279711

*Element, type=S4
  1,   1,  19, 525,  62
  2,  19,  20, 526, 525

4751, 212, 523, 524, 213
4752, 213, 524,   9,   8

*Element, type=S4R
 379,   15,  245,  785,  395
 380,  245,  246,  786,  785

4724, 4859, 4860,  342,  341
4725, 4860,  498,   16,  342

*Nset, nset=_PickedSet19, internal, generate
    1,  4860,     1
*Elset, elset=_PickedSet19, internal, generate
    1,  4752,     1
*Nset, nset=_PickedSet25, internal, generate
    1,  4860,     1
*Elset, elset=_PickedSet25, internal, generate
    1,  4752,     1
*Nset, nset=_PickedSet28, internal, generate
    1,  4860,     1
```

```
*Elset, elset=_PickedSet28, internal, generate
    1,  4752,     1
*Nset, nset=_PickedSet35, internal, generate
    1,  4860,     1
*Elset, elset=_PickedSet35, internal, generate
    1,  4752,     1
*Nset, nset=_PickedSet37, internal
   2,   3,   4,   7,   8,   9,  10,  11,  12,  17,  24,  25,  26,
27,  28,  29


 4741, 4742, 4743, 4744, 4745, 4746, 4747, 4748, 4749, 4750,
4751, 4752

*Nset, nset=_PickedSet38, internal
    1,    2,    3,    4,    5,    6,    8,   11,   13,   14,
15,   16,   18,   19,   20,   21

 4845, 4846, 4847, 4848, 4849, 4850, 4851, 4852, 4853, 4854,
4855, 4856, 4857, 4858, 4859, 4860

*Elset, elset=_PickedSet38, internal
    1,    2,    3,    4,    5,    6,    7,    8,    9,   10,
11,   12,   13,   14,   15,   16

4716, 4717, 4718, 4719, 4720, 4721
 4722, 4723, 4724, 4725

*Nset, nset=_PickedSet39, internal, generate
    1,  4860,     1
*Elset, elset=_PickedSet39, internal, generate
    1,  4752,     1
** Region: (SevenTube:Picked), (Controls:EC-1), (Material
Orientation:Picked)
*Elset, elset=_I1, internal
    1,    2,    3,    4,    5,    6,    7,    8,    9,   10,
11,   12,   13,   14,   15,   16

2714, 2715, 2716, 2717, 2718, 2719
 2720, 2721, 2722, 2723, 2724, 2725, 2726, 2727
** Section: SevenTube
*Shell Section, elset=_I1, composite, controls=EC-1, layup="All
Layers"
0.0001307, 1, T700/QY8911, 45.
0.0001307, 1, T700/QY8911, -45.
0.0001307, 1, T700/QY8911, 90.
0.0001307, 1, T700/QY8911, 0.
0.0001307, 1, T700/QY8911, 0.
0.0001307, 1, T700/QY8911, 90.
0.0001307, 1, T700/QY8911, 0.
** Section: Trigger
```

```
*Shell Section, elset=_PickedSet37, composite, controls=EC-1,
offset=SPOS, layup=Trigger
0.0001307, 1, T700/QY8911, 45.
0.0001307, 1, T700/QY8911, -45.
0.0001307, 1, T700/QY8911, 0.
0.0001307, 1, T700/QY8911, 90.
** Region: (SevenTube:Picked), (Controls:EC-2), (Material
Orientation:Picked)
*Elset, elset=_I3, internal
  379,  380,  381,  382,  383,  384,  385,  386,  387,  388,
389,  390,  391,  392,  393,  394

 4714, 4715, 4716, 4717, 4718, 4719, 4720, 4721, 4722, 4723,
4724, 4725

** Section: SevenTube
*Shell Section, elset=_I3, composite, controls=EC-2, layup="All
Layers"
0.0001307, 1, T700/QY8911, 45.
0.0001307, 1, T700/QY8911, -45.
0.0001307, 1, T700/QY8911, 90.
0.0001307, 1, T700/QY8911, 0.
0.0001307, 1, T700/QY8911, 0.
0.0001307, 1, T700/QY8911, 90.
0.0001307, 1, T700/QY8911, 0.
*End Part
**
**
** ASSEMBLY
**
*Assembly, name=Assembly
**
*Instance, name=Base-1, part=Base
*Node
      1,           0.,           0.,           0.
*Nset, nset=Base-1-RefPt_, internal
1,
*Surface, type=REVOLUTION, name=RigidSurface_, internal
START,           0.,           0.
 LINE,        0.027,           0.
 LINE,        0.027,         0.01
 LINE,        0.047,         0.01
 LINE,        0.047,           0.
 LINE,        0.097,           0.
*Rigid Body, ref node=Base-1-RefPt_, analytical
surface=RigidSurface_
*End Instance
**
*Instance, name=Tube-1, part=Tube
          0.,           0.,           0.
          0.,           0.,           0.,          -1.,
0.,           0.,          90.
```

```
*End Instance
**
*Instance, name=Impactor-1, part=Impactor
          0.,       0.1004,           0.
*Node
      1,           0.,           0.,           0.
*Nset, nset=Impactor-1-RefPt_, internal
1,
*Nset, nset=_PickedSet3, internal
 1,
*Surface, type=CYLINDER, name=RigidSurface_, internal
START,          0.1,           0.
 LINE,         -0.1,           0.
*Rigid Body, ref node=Impactor-1-RefPt_, analytical
surface=RigidSurface_
*Element, type=MASS, elset=_PickedSet3_ImpactorInertia_
1, 1
*Mass, elset=_PickedSet3_ImpactorInertia_
100.,
*End Instance
**
*Instance, name=OuterTube-1, part=OuterTube
          0.,           0.,           0.
          0.,           0.,           0.,          -1.,
0.,           0.,          90.
*End Instance
**
*Nset, nset=_PickedSet10, internal, instance=Base-1
 1,
*Nset, nset=_PickedSet11, internal, instance=Impactor-1
 1,
*Nset, nset=_PickedSet12, internal, instance=Impactor-1
 1,
*Nset, nset=ImpactorSet, instance=Impactor-1
 1,
*Nset, nset=BaseSet, instance=Base-1
 1,
*Nset, nset=_PickedSet26, internal, instance=Tube-1
  15,  16,  18, 343, 344, 345, 346, 347, 348, 349, 350, 351, 352,
353, 354, 355

 487, 488, 489, 490, 491, 492, 493, 494, 495, 496, 497, 498

*Elset, elset=_PickedSet26, internal, instance=Tube-1
  379,  416,  453,  490,  527,  564,  601,  638,  675,  712,
749,  786,  823,  860,  897,  934

 4318, 4355, 4392, 4429, 4466, 4503, 4540, 4577, 4614, 4651,
4688, 4725

*Nset, nset=TubeSet, instance=Tube-1
```

```
    1,    5,    6,   13,   14,   15,   16,   18,   54,   55,
56,   57,   58,   59,   60,   61

4847, 4848, 4849, 4850, 4851, 4852
 4853, 4854, 4855, 4856, 4857, 4858, 4859, 4860

*Elset, elset=TubeSet, instance=Tube-1
  379,  380,  381,  382,  383,  384,  385,  386,  387,  388,
389,  390,  391,  392,  393,  394

 4714, 4715, 4716, 4717, 4718, 4719, 4720, 4721, 4722, 4723,
4724, 4725

*Nset, nset=_PickedSet54, internal, instance=Impactor-1
 1,
*Elset, elset=__PickedSurf24_SPOS, internal, instance=Tube-1
  379,  380,  381,  382,  383,  384,  385,  386,  387,  388,
389,  390,  391,  392,  393,  394

 4714, 4715, 4716, 4717, 4718, 4719, 4720, 4721, 4722, 4723,
4724, 4725
*Surface, type=ELEMENT, name=_PickedSurf24, internal
__PickedSurf24_SPOS, SPOS
*Elset, elset=__PickedSurf44_SNEG, internal, instance=Tube-1
  379,  380,  381,  382,  383,  384,  385,  386,  387,  388,
389,  390,  391,  392,  393,  394

4714, 4715, 4716, 4717, 4718, 4719, 4720, 4721, 4722, 4723, 4724,
4725
*Surface, type=ELEMENT, name=_PickedSurf44, internal
__PickedSurf44_SNEG, SNEG
*Elset, elset=__PickedSurf45_SPOS, internal, instance=OuterTube-1
  337,  338,  339,  340,  341,  342,  343,  344,  345,  346,
347,  348,  349,  350,  351,  352

4773, 4774, 4775, 4776, 4777, 4778, 4779, 4780, 4781, 4782, 4783,
4784, 4785, 4786, 4787, 4788
*Surface, type=ELEMENT, name=_PickedSurf45, internal
__PickedSurf45_SPOS, SPOS
*Elset, elset=__PickedSurf46_SPOS, internal, instance=OuterTube-1
  337,  338,  339,  340,  341,  342,  343,  344,  345,  346,
347,  348,  349,  350,  351,  352

 4773, 4774, 4775, 4776, 4777, 4778, 4779, 4780, 4781, 4782,
4783, 4784, 4785, 4786, 4787, 4788

*Surface, type=ELEMENT, name=_PickedSurf46, internal
__PickedSurf46_SPOS, SPOS
*Elset, elset=__PickedSurf47_SPOS, internal, instance=Tube-1
  379,  380,  381,  382,  383,  384,  385,  386,  387,  388,
389,  390,  391,  392,  393,  394
```

```
 4714, 4715, 4716, 4717, 4718, 4719, 4720, 4721, 4722, 4723,
4724, 4725

*Surface, type=ELEMENT, name=_PickedSurf47, internal
__PickedSurf47_SPOS, SPOS
*Elset, elset=__PickedSurf48_SNEG, internal, instance=OuterTube-1
  337,  338,  339,  340,  341,  342,  343,  344,  345,  346,
347,  348,  349,  350,  351,  352

 4773, 4774, 4775, 4776, 4777, 4778, 4779, 4780, 4781, 4782,
4783, 4784, 4785, 4786, 4787, 4788
*Surface, type=ELEMENT, name=_PickedSurf48, internal
__PickedSurf48_SNEG, SNEG
*Elset, elset=__PickedSurf49_SPOS, internal, instance=OuterTube-1
  337,  338,  339,  340,  341,  342,  343,  344,  345,  346,
347,  348,  349,  350,  351,  352

 4773, 4774, 4775, 4776, 4777, 4778, 4779, 4780, 4781, 4782,
4783, 4784, 4785, 4786, 4787, 4788
*Surface, type=ELEMENT, name=_PickedSurf49, internal
__PickedSurf49_SPOS, SPOS
*Surface, type=NODE, name=_PickedSet26_CNS_, internal
_PickedSet26, 1.
** Constraint: OuterToBaseTie
*Tie, name=OuterToBaseTie, adjust=yes, no rotation
_PickedSurf49, Base-1.RigidSurface_
** Constraint: TubeToBaseTie
*Tie, name=TubeToBaseTie, adjust=yes, no rotation
_PickedSet26_CNS_, Base-1.RigidSurface_
*End Assembly
**
** ELEMENT CONTROLS
**
*Section Controls, name=EC-1, ELEMENT DELETION=YES, MAX
DEGRADATION=0.5
1., 1., 1.
*Section Controls, name=EC-2, ELEMENT DELETION=YES, MAX
DEGRADATION=0.8, hourglass=STIFFNESS
1., 1., 1.
*Section Controls, name=EC-3, ELEMENT DELETION=YES, MAX
DEGRADATION=0.65
1., 1., 1.
**
** MATERIALS
**
*Material, name=T700/QY8911
*Damage Initiation, criterion=HASHIN, alpha=1.
 2.326e+09, 1.236e+09,   5.1e+07,  2.09e+08,  8.79e+07,  8.79e+07
*Damage Evolution, type=ENERGY
 2.2044e+07, 6.2238e+06,    156859., 2.6345e+06
*Density
 1.53e+07,
```

```
*Elastic, type=LAMINA
 1.35e+11, 9.12e+09,    0.021, 5.67e+09, 5.67e+09, 5.67e+09
**
** INTERACTION PROPERTIES
**
*Surface Interaction, name=IntProp-1
*Friction
 0.2,
*Contact Damping, definition=CRITICAL DAMPING FRACTION
0.5,
*Surface Interaction, name=IntProp-2
**
** BOUNDARY CONDITIONS
**
** Name: BaseBC Type: Displacement/Rotation
*Boundary
_PickedSet10, 1, 1
_PickedSet10, 2, 2
_PickedSet10, 3, 3
_PickedSet10, 4, 4
_PickedSet10, 5, 5
_PickedSet10, 6, 6
** Name: ImpactorBC Type: Displacement/Rotation
*Boundary
_PickedSet11, 1, 1
_PickedSet11, 3, 3
_PickedSet11, 4, 4
_PickedSet11, 5, 5
_PickedSet11, 6, 6
**
** PREDEFINED FIELDS
**
** Name: ImpactorInitialVel   Type: Velocity
*Initial Conditions, type=VELOCITY
_PickedSet12, 1, 0.
_PickedSet12, 2, -0.01
_PickedSet12, 3, 0.
** ----------------------------------------------------------------
--
**
** STEP: Step-1
**
*Step, name=Step-1
*Dynamic, Explicit, element by element
, 0.31
*Bulk Viscosity
0.5, 1.2
**
** BOUNDARY CONDITIONS
**
** Name: ImpactorAcc Type: Acceleration/Angular acceleration
*Boundary, type=ACCELERATION
```

```
_PickedSet54, 2, 2, -1.
**
** INTERACTIONS
**
** Interaction: BaseToOuter
*Contact Pair, interaction=IntProp-1, mechanical
constraint=PENALTY, cpset=BaseToOuter
Base-1.RigidSurface_, _PickedSurf45
** Interaction: BaseToTubeS
*Contact Pair, interaction=IntProp-1, mechanical
constraint=PENALTY, cpset=BaseToTubeS
Base-1.RigidSurface_, _PickedSurf24
** Interaction: ImpactorToOuter
*Contact Pair, interaction=IntProp-1, mechanical
constraint=PENALTY, cpset=ImpactorToOuter
Impactor-1.RigidSurface_, _PickedSurf46
** Interaction: ImpactorToTubeS
*Contact Pair, interaction=IntProp-1, mechanical
constraint=PENALTY, cpset=ImpactorToTubeS
Impactor-1.RigidSurface_, _PickedSurf44
** Interaction: InnerToOuter
*Contact Pair, interaction=IntProp-1, mechanical
constraint=PENALTY, cpset=InnerToOuter
_PickedSurf47, _PickedSurf48
** Interaction: SelfContactS
*Contact, op=NEW
*Contact Inclusions, ALL EXTERIOR
*Contact Property Assignment
 ,  , IntProp-2
**
** OUTPUT REQUESTS
**
*Restart, write, number interval=1, time marks=NO
**
** FIELD OUTPUT: F-Output-3
**
*Output, field, time interval=0.005
*Node Output
U,
*Element Output, directions=YES
DMICRT, E, S, STATUS
**
** FIELD OUTPUT: F-Output-2
**
*Node Output, nset=ImpactorSet
U,
**
** FIELD OUTPUT: F-Output-1
**
*Output, field, variable=PRESELECT, time interval=0.005
**
** HISTORY OUTPUT: H-Output-4
```

```
**
*Output, history, time interval=0.005
*Energy Output
ALLAE, ALLKE, ALLPD, ALLSE, ALLWK, ETOTAL
**
** HISTORY OUTPUT: H-Output-1
**
*Output, history, variable=PRESELECT, time interval=0.005
**
** HISTORY OUTPUT: H-Output-3
**
*Output, history, time interval=0.01
*Node Output, nset=BaseSet
RF2,
**
** HISTORY OUTPUT: H-Output-2
**
*Node Output, nset=ImpactorSet
U2,
*End Step
```